JOURNAL OF GEOPHYSICAL RESEARCH, VOL. 115, F03005, doi:10.1029/2009JF001514, 2010

Click Here for Full Article

The perfect debris flow? Aggregated results from 28 large-scale experiments

Richard M. Iverson,[1] Matthew Logan,[1] Richard G. LaHusen,[1] and Matteo Berti[1,2]

Received 4 September 2009; revised 22 January 2010; accepted 1 March 2010; published 10 July 2010.

[1] Aggregation of data collected in 28 controlled experiments reveals reproducible debris-flow behavior that provides a clear target for model tests. In each experiment ~10 m^3 of unsorted, water-saturated sediment composed mostly of sand and gravel discharged from behind a gate, descended a steep, 95-m flume, and formed a deposit on a nearly horizontal runout surface. Experiment subsets were distinguished by differing basal boundary conditions (1 versus 16 mm roughness heights) and sediment mud contents (1 versus 7 percent dry weight). Sensor measurements of evolving flow thicknesses, basal normal stresses, and basal pore fluid pressures demonstrate that debris flows in all subsets developed dilated, coarse-grained, high-friction snouts, followed by bodies of nearly liquefied, finer-grained debris. Mud enhanced flow mobility by maintaining high pore pressures in flow bodies, and bed roughness reduced flow speeds but not distances of flow runout. Roughness had these effects because it promoted debris agitation and grain-size segregation, and thereby aided growth of lateral levees that channelized flow. Grain-size segregation also contributed to development of ubiquitous roll waves, which had diverse amplitudes exhibiting fractal number-size distributions. Despite the influence of these waves and other sources of dispersion, the aggregated data have well-defined patterns that help constrain individual terms in a depth-averaged debris-flow model. The patterns imply that local flow resistance evolved together with global flow dynamics, contradicting the hypothesis that any consistent rheology applied. We infer that new evolution equations, not new rheologies, are needed to explain how characteristic debris-flow behavior emerges from the interactions of debris constituents.

Citation: Iverson, R. M., M. Logan, R. G. LaHusen, and M. Berti (2010), The perfect debris flow? Aggregated results from 28 large-scale experiments, *J. Geophys. Res.*, *115*, F03005, doi:10.1029/2009JF001514.

1. Introduction

[2] Detailed data are necessary for testing models used to interpret and predict debris-flow behavior, but data well-suited for this purpose are rare. The utility of field data is typically limited by unknown or irreproducible initial and boundary conditions and poorly constrained material properties, and the utility of laboratory data is typically limited by scaling problems resulting from the small size of experimental flows. Data from large-scale laboratory debris flows also have limitations, because feedbacks between grain-scale mechanics and macroscopic mechanics can cause some aspects of flow behavior to be idiosyncratic or even chaotic. In contrast, a perfect debris flow - one ideally suited to guide model formulation and testing - would lack idiosyncrasies and instead represent an ensemble average. That is, it would represent the mean behavior of a population of flows that develop from macroscopically identical initial states.

[3] In this paper we present and interpret data that are well-suited for testing both the conceptual underpinnings and quantitative predictions of debris-flow models. We obtain these data by aggregating the results of 28 large-scale experiments conducted at the USGS debris-flow flume from 1994 to 2004 (Figure 1). The experiments involved unsteady, nonuniform debris-flow motion from initiation to deposition, and thus differed greatly from experiments aimed at measuring debris rheology in steady states. Although all of the experiments had the same initial configuration, subsets had differing basal boundary conditions (smooth or rough concrete beds) and debris compositions (water-saturated sand and gravel with or without a significant fraction of mud-sized grains <0.0625 mm). The experiments with a rough bed and significant mud most closely mimicked conditions in natural debris flows, but the other experiments demonstrated how a lack of mud or bed roughness can influence flow dynamics.

[4] For each subset of experiments, we present aggregated time series that depict the evolving means and standard deviations of flow thicknesses, basal normal stresses, and

[1]U.S. Geological Survey, Cascade Volcano Observatory, Vancouver, Washington, USA.
[2]Now at Dipartimento di Scienze della Terra e Geologico-Ambientali, Università di Bologna, Bologna, Italy.

Copyright 2010 by the American Geophysical Union.
0148-0227/10/2009JF001514

Figure 1. Photograph of a 10 m^3 debris flow descending the USGS debris-flow flume at the H. J. Andrews Experimental Forest near Blue River, Oregon.

basal pore fluid pressures measured as debris flows passed three instrumented cross sections. We also present data on debris properties, flow-front velocities, deposit geometries, and surface waves that resulted from flow instabilities. The time series data are accessible in digital form in the auxiliary material, and they are supplemented by extensive video documentation of the experiments, which is viewable online [*Logan and Iverson*, 2007].[1]

2. Theoretical Background and Scaling

[5] To provide a context for our data collection and interpretation, we briefly review the elements of a one-dimensional, depth-averaged model of a two-phase debris flow descending a uniform slope (Figure 2). The model illustrates the interdependence of some key quantities measured in our experiments, and it provides a framework for evaluating the effects of debris-flow scale, an important consideration in our experiment design.

[1]Auxiliary material data sets are available at ftp://ftp.agu.org/apend/jf/2009jf001514.

2.1. Depth-Averaged Dynamics

[6] The model treats a debris flow as a finite mass of incompressible solid grains of density ρ_s mixed with incompressible viscous pore fluid of density ρ_f, such that the mixture bulk density is $\rho = \rho_s(1 - n) + \rho_f n$, where n is the porosity or fluid volume fraction. Evolution of n (and corresponding evolution of ρ) can be accompanied by significant changes in pore fluid pressure, p, owing to generally small values of the hydraulic diffusivity D that regulates pore pressure equilibration in dilating or contracting debris [*Iverson*, 1997; *Iverson et al.*, 2000; *Major*, 2000]. The model includes ρ and D as depth-averaged quantities but lacks differential equations governing their evolution. The resulting lack of mathematical closure can be circumvented by treating ρ and D as constants or as specified functions of other variables [e.g., *Iverson and Denlinger*, 2001; *Denlinger and Iverson*, 2001; *Savage and Iverson*, 2003], but our experiments test whether such simplifications are warranted.

[7] The model's governing equations describe simultaneous evolution of the flow thickness, h, depth-averaged flow velocity, v, and basal pore fluid pressure, p_{bed}, all as functions of the downslope distance x and time t:

$$\frac{dh}{dt} = -h\frac{\partial v}{\partial x} - \frac{h}{\rho}\frac{d\rho}{dt} \tag{1}$$

$$\rho h\frac{dv}{dt} = \rho g h\left[\sin\theta - \kappa\cos\theta\frac{\partial h}{\partial x}\right] - h(1-\kappa)\frac{\partial p_{bed}}{\partial x} - \tau_s - \tau_f \tag{2}$$

$$\frac{dp_{bed}}{dt} = -\frac{2D}{h}\left(\frac{p_{bed}}{h} - \rho_f g\cos\theta\right) + g\cos\theta\frac{d(\rho h)}{dt}. \tag{3}$$

Here d/dt is a Lagrangian time derivative defined as $d/dt = \partial/\partial t + v\partial/\partial x$, g is the magnitude of gravitational acceleration, θ is the angle of bed inclination, κ is a longitudinal normal-

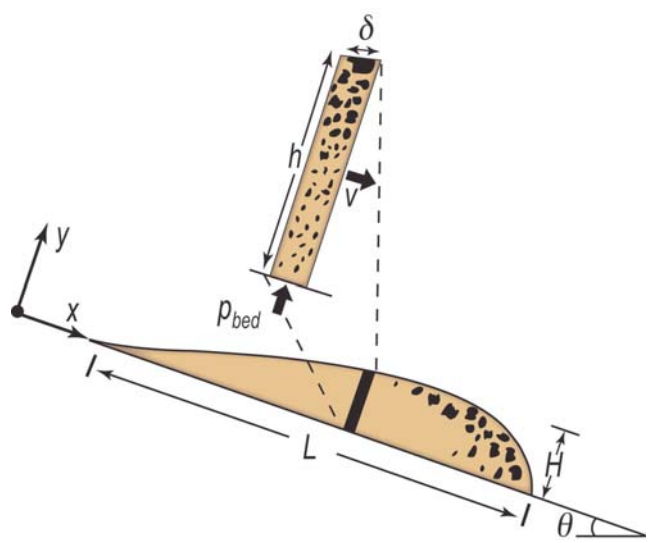

Figure 2. Schematic vertical cross section of a debris flow descending a uniform slope inclined at the angle θ. The $x - y$ coordinate system and flow length scales H and L are defined. Magnified slice illustrates the dependent variables, v, h and p_{bed} as well as a local grain length scale, δ.

stress coefficient (of order 1), τ_s is the basal shear stress exerted by solid grains, and τ_f is the basal shear stress exerted by pore fluid. In (3) the term containing D is a surrogate for a conventional pore pressure diffusion term, $D(\partial^2 p/\partial y^2)$, because the depth-averaged formulation includes no explicit description of variations of any quantity in the y direction, normal to x (Appendix A). Among the model equations, (2) is the most important for guiding experiment design and data interpretation, because it demonstrates that evolution of flow momentum involves interaction of v, h, and p_{bed}, as well as the effects of ρ, D, and stress. Here we briefly summarize stress estimation as a guide for scaling and similitude; we describe empirical stress evaluation in section 7 (Implications for Modeling).

[8] We estimate the solid-phase basal shear stress τ_s by combining the *Terzaghi* [1925] effective-stress principle with a modified *Coulomb* [1773] equation for granular friction to obtain

$$\tau_s = [\sigma_{bed} - p_{bed}] \tan \phi_{bed}(S), \tag{4}$$

where σ_{bed} is the total basal normal stress (estimated as $\rho g h \cos\theta$), $\sigma_{bed} - p_{bed}$ is the effective basal normal stress, and ϕ_{bed} is the basal friction angle, which may be an increasing function of the Savage number, S (or of its square root, the inertia number) [cf. *Ancey and Evesque*, 2000; *GDR MiDi Group*, 2004; *Forterre and Pouliquen*, 2008]. The Savage number expresses the characteristic ratio of grain-scale inertial stresses caused by shearing to bulk-scale intergranular stress caused by gravity, and for debris flows it may be defined as

$$S = \frac{\rho_s \dot{\gamma}^2 \delta^2}{\sigma_{bed} - p_{bed}}, \tag{5}$$

where $\dot{\gamma}$ is the characteristic shear rate, and δ is the characteristic grain diameter [*Iverson and Vallance*, 2001]. In a debris flow $\dot{\gamma}$ and δ can vary considerably, but for estimation purposes we approximate $\dot{\gamma}$ by its local depth-averaged value ($\dot{\gamma} \approx v/h$), and we approximate δ by the effective (sieve) diameter of grains locally constituting the debris' modal mass fraction.

[9] We use $\dot{\gamma} \approx v/h$ also to estimate the fluid-phase contribution to basal shear stress in (2) as:

$$\tau_f = \tau_y + \mu \frac{v}{h}. \tag{6}$$

This equation, similar in form to a one-dimensional Bingham equation [*Bingham and Green*, 1919], represents the effects of fluid yield stress τ_y (typically <400 Pa in debris-flow mixtures) as well as fluid viscosity μ (typically <50 Pa-s) [*Iverson*, 2003].

[10] We estimate values of the longitudinal normal-stress coefficient, κ, in (2) by considering two-dimensional *Rankine* [1857] states similar to those used in soil mechanics to compute lateral earth-pressure coefficients [*Lambe and Whitman*, 1979, pp. 162–194]. Thus, for Coulomb debris that fails internally (with an internal friction angle ϕ_{int}) as it slides along a rigid bed (with a friction angle ϕ_{bed}), κ can assume either of two values given by

$$\kappa = 2\frac{1 \mp [1 - \cos^2\phi_{\text{int}}(1 + \tan^2\phi_{bed})]^{1/2}}{\cos^2\phi_{\text{int}}} - 1, \tag{7}$$

where the $-$ in $\mp$ applies in regions with diverging flow ($\partial v/\partial x > 0$), and $+$ applies in regions with converging flow ($\partial v/\partial x < 0$) [*Savage and Hutter*, 1989; *Iverson*, 1997]. Equation (7) implies that $\phi_{bed} \le \phi_{\text{int}}$; otherwise no slip occurs at the bed and ϕ_{bed} is irrelevant. For the important limiting case in which $\phi_{bed} = \phi_{\text{int}}$ (which applies to self-formed, rough beds), (7) reduces to an equation like that describing the ratio of slope-parallel and slope-normal compressive stresses in homogeneous infinite slopes obeying Coulomb limiting equilibrium throughout:

$$\kappa = \frac{1 + \sin^2\phi_{\text{int}}}{1 - \sin^2\phi_{\text{int}}}. \tag{8}$$

The contrast between this single-valued expression for κ and the dual-valued expression applicable if $\phi_{bed} \le \phi_{\text{int}}$ (i.e., (7)) implies that differences in bed roughness can have effects beyond those of simple differences in basal shear resistance.

2.2. Scaling and Similitude

[11] Dynamic similarity of experimental and full-sized debris flows demands two kinds of scaling: that for flow as a whole, where the pertinent length scales are the characteristic height H and length L of a surge of debris, and that for grain-scale mechanics that generate stresses, where the pertinent length scale is δ (Figure 2). Here we show how whole-flow scaling arises from normalization of (1)–(3), and we link whole-flow dynamics to grain-scale dynamics through the quantities S and δ/H.

[12] Our normalization of (1)–(3) follows that of *Savage and Iverson* [2003] by employing the following fundamental scales for distance, time, and the dependent variables v, h, and p_{bed}: $x \sim L$, $t \sim \sqrt{L/g}$, $v \sim \sqrt{gL}$, $h \sim H$, $p_{bed} \sim \rho_0 g H \cos\theta$. (Here ρ_0 is a reference value of ρ, such as the value at static, limiting equilibrium.) Use of these scales in (1)–(3), with (4)–(6) embedded, shows that the dynamics described by (1)–(3) is controlled by seven dimensionless quantities in addition to θ and κ (Appendix B):

$$\varepsilon = \frac{H}{L} \qquad R = \frac{\rho}{\rho_0} \qquad R_f = \frac{\rho_f}{\rho_0} \qquad C = \frac{\tau_s}{\rho_0 g H} \qquad Y = \frac{\tau_y}{\rho_0 g H}$$
$$N_R = \frac{\rho_0 H \sqrt{gL}}{\mu} \qquad N_P = \frac{\sqrt{L/g}}{H^2/D}. \tag{9}$$

The definitions of ε, R, and R_f involve simple ratios of lengths and densities that must be maintained to establish similitude, but they imply no inherent scale-dependence. (Typically, $\varepsilon \ll 1$, $R \approx 1$, and $R_f \approx 0.6$ for debris flows of any scale.) Likewise, the definition of C implies little inherent scale-dependence, because τ_s depends on the effective normal stress, which scales with $\rho_0 g H$, and on ϕ, which is nearly constant. In contrast, the definition of Y indicates a clear scale-dependence, because only its denominator increases as H increases. Effects of fluid yield strength τ_y can thus be expected to decrease as debris-flow size increases.

[13] The last two parameters defined in (9), N_R and N_P, reveal that scale-dependent effects of pore fluid viscosity μ pose severe problems for similitude. The parameter N_R is a Reynolds number in which the characteristic velocity is

Table 1. Values of Dimensionless Scaling Parameters for Three Geometrically Similar Debris Flows of Identical Composition but Differing Sizes Expressed by H Values[a]

Dimensionless Scaling Parameter	Bench-Top Flow $H = 0.03$ m	USGS Flume Flow $H = 0.3$ m	Full-Scale Flow $H = 3$ m
ε	0.01	0.01	0.01
R	1	1	1
R_f	0.6	0.6	0.6
C	0–0.5	0–0.5	0–0.5
Y	0.2	0.02	0.002
N_R	3×10^3	1×10^5	3×10^6
N_P	6×10^{-3}	2×10^{-4}	6×10^{-6}
δ/H	0.3	0.03	0.003
S	10	0.1	0.001

[a]Debris composition is specified by the parameter values: $\delta = 0.01$ m, $\rho_0 = 2000$ kg/m^3, $\rho_s = 2700$ kg/m^3, $\rho_f = 1200$ kg/m^3, $\tau_y = 100$ Pa, $\mu = 0.1$ Pa-s, $D = 10^{-5}$ m^2/s.

$\sqrt{gL}$; its definition shows that effects of μ on bulk shear resistance decrease as debris-flow size increases. The definition can be rewritten as $N_R = \rho_0(g/\varepsilon)^{1/2}H^{3/2}/\mu$, a form implying that the effect of μ on shear resistance in geometrically similar debris flows (with ε constant) is inversely proportional to $H^{3/2}$. Likewise, the definition of N_P, which expresses the ratio of timescales for debris-flow motion and pore pressure diffusion, can be rewritten as $N_P = kE/[(\varepsilon g)^{1/2}H^{3/2}\mu]$, a form demonstrating that the effect of μ on maintenance of p_{bed} is directly proportional to $H^{3/2}$. (Here k is the intrinsic hydraulic permeability of the debris, E is its bulk stiffness modulus, and $kE/\mu = D$.) Thus, the combination of N_R scaling and N_P scaling implies that the effects of μ on bulk shear resistance and pore pressure persistence diverge at the rate H^3 increases.

[14] Values of scaling parameters calculated for geometrically similar debris flows of differing sizes demonstrate that dynamic similarity over a broad range of scales is probably unattainable (Table 1). For example, miniature debris flows are likely to exhibit disproportionately large effects of fluid yield strength, viscous flow resistance, and grain inertia, while exhibiting disproportionately little effect of pore fluid pressure. Such difficulties provide motivation for conducting debris-flow experiments at the largest scale possible, prompting our construction and use of the USGS debris-flow flume. Experiments in the flume provide full-scale analogs of modest-sized natural debris flows, and their size also promotes similarity with larger debris flows (Table 1).

3. Experiment Configuration and Materials

3.1. Flume Geometry and Bed Roughness

[15] The USGS debris-flow flume is a straight, rectangular concrete channel 95 m long, 2 m wide, and 1.2 m deep. Longitudinal distances in the flume (x) are referenced not to its upper end but instead to a position 12.5 m downslope, where a 2-m high vertical headgate is used to retain static debris prior to its release (Figure 3a). Throughout most of its length the flume bed slopes uniformly at $\theta = 31°$, comparable to the angles of many debris-flow initiation sites [*Iverson et al.*, 1997]. At $x = 74$ m the flume bed begins to flatten, and beyond this point it follows a catenary curve that descends 2.2 m vertically before reaching the flume mouth, where $x = 82.5$ m and $\theta = 4°$. There, the flume debouches onto a nearly planar concrete runout surface that slopes 2.4° away from the flume, on average (Figure 3b). The concrete runout surface extends to $x = 107.5$ m, although the distal 11-m section of this surface was not in place in the two earliest (1994) experiments we report here. The steep slope and wide channel of the flume encourage development of nearly one-dimensional flow, whereas the unconfined runout surface permits lateral spreading of debris prior to deposition.

[16] All flows in the flume are subtly influenced by a construction flaw that causes the bed to tilt slightly to the left as viewed by an observer facing downslope. Theodolite measurements show that the flaw is detectable in most sections of the flume but is most pronounced from $x = 36$ m to $x = 75$ m, where the leftward tilt averages about 2°. Not easily remedied, this tilt is in some respects fortuitous because it reveals flow sensitivity to nuances in bed slope.

[17] In all of our experiments prior to September 2000, the flume bed had a smoothly broomed concrete surface like that of a standard sidewalk, but in 2000 we covered the surface from $x = 6$ m to $x = 79$ m with bumpy concrete tiles that significantly increased the bed roughness. The pattern and amplitude of bumpiness were chosen so that our sediment mixtures, when placed on the bed, had basal angles of repose matching their internal angles of repose of 39–40°. (See section 3.4 below on Sediment Geotechnical Properties.) We attained matched angles of repose by using tiles covered with regularly spaced, rounded conical bumps, each 16 mm high and 3 cm in diameter, with apexes spaced 5 cm apart (Figure 4). We did not install bumpy tiles in the area immediately downslope of the headgate ($x < 6$ m) or in the runout area at the base of the flume ($x > 79$ m), because in these locations tiles would have impeded capture of water that leaked from the headgate and complicated removal of sediment during experiment clean-up.

3.2. Sediment Textures

[18] We designate the two sediment mixtures used in our experiments as sand-gravel (SG) and sand-gravel-mud (SGM), where mud refers to all grains passing a 0.0625 mm mesh during wet-sieving. A local sand-gravel retailer prepared each mixture to our specifications, and the resulting SG batches had relatively consistent textures: on average 66 percent gravel, 33 percent sand, and 1 percent mud by dry weight (Figure 5a). The SGM mixtures were more variable because they were created by blending 80 percent SG with 20 percent unsorted loam excavated from the floodplain of the Willamette River near Eugene, Oregon. The resulting SGM textures averaged 56 percent gravel, 37 percent sand, and 7 percent mud by dry weight (Figure 5b). Sedigraph analyses of the mud fraction showed that less than 1/3 of its mass generally consisted of clay-sized particles. Both the SG and SGM mixtures had modal concentrations of grains in the 8–32 mm size classes and secondary modal peaks in the 0.25 to 0.5 mm size class. Most of the gravel-sized grains in both mixtures were rounded and moderately bladed in form, whereas the sand was mostly sub-angular and of mixed form. *Major* [1996, 1997, 1998] provided more-detailed sedimentological descriptions of these materials, although he considered a subset of experiments and sediment samples different from ours.

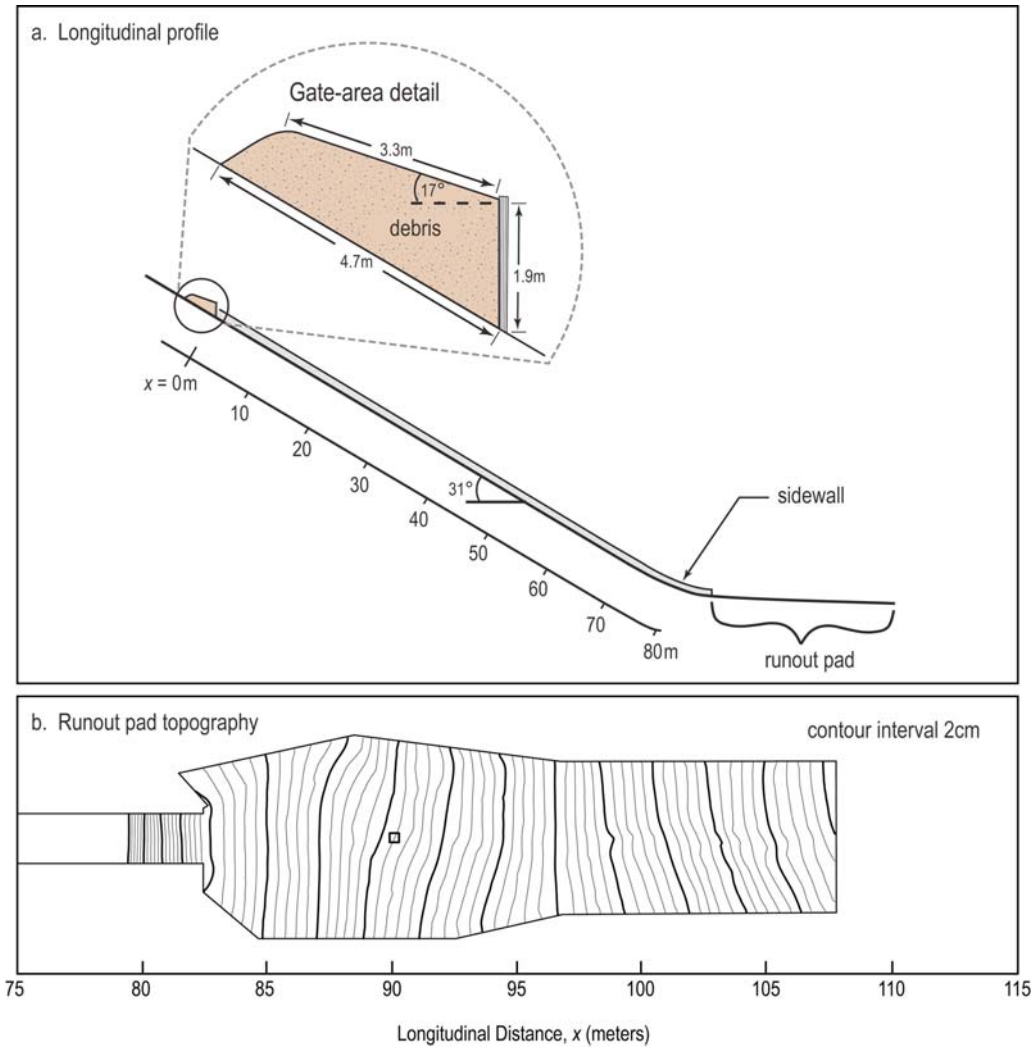

Figure 3. Flume geometry. (a) Longitudinal profile of flume and adjacent runout pad. Magnified segment shows geometry of static debris loaded behind the headgate. (b) Topographic map of the concrete runout pad. Square at x = 90 m depicts location of instrumentation port.

3.3. Sediment Preparation and Water Application

[19] In preparation for each experiment, we placed a wedge-shaped prism of loosely packed, static sediment behind the flume headgate. The prism volumes were 9.7 ± 0.4 m^3, where the ± value denotes 1 standard deviation from the mean for the 8 to 11 experiments in each subset (Table 2). The geometries of the prisms were similarly standardized, with surfaces graded to have uniform slopes of about 17° except at their upslope ends, where they were bluntly truncated (Figure 3a).

[20] Placement of the sediment prisms involved a combination of dumping from a front-end loader and manual shoveling and raking. As a result, the sediment was affected by some random foot traffic, but no systematic compaction was intended or attempted. Some grain-size segregation occurred during each dump of the loader bucket, but we redistributed the sediment to eliminate conspicuous gravel accumulations and make the mixture macroscopically homogeneous.

[21] Sediment sampling and analysis showed that dry bulk densities of both the SG and SGM loaded behind the headgate averaged about 1700 ± 100 kg/m^3, and the native water contents averaged about 6% for the SG and 8% for the SGM (Table 2). The dry bulk densities implied typical sediment porosities of about 0.37, although sample variability indicated that porosities ranging from about 0.32 to 0.43 were plausible.

[22] After we measured and sampled the sediment prisms, we watered them using a metered distribution system that included both subsurface channels and surface sprinklers. The prisms typically contained about 1.0 to 1.1 m^3 of native water in their initial state, and we typically applied an additional 2.0 to 2.2 m^3 of water to attain a final state of near-saturation. Watering generally required 2 to 6 h, depending on sediment mud content and water leakage through the headgate. (We sealed the headgate by applying expanding polyurethane foam to all joints and hinge lines prior to sediment loading, but the seal was sometimes imperfect.) Table 2

Figure 4. Photograph of tiled bumpy flume bed and two instrumentation ports at nominal x = 66 m. Steel plates (black) covering ports have lengths and widths of 34 cm, and circular load-cell plates (green) installed in the ports have diameters of 25.2 cm.

summarizes the water-budget data, and Appendix C details the methods used to compute the budget.

3.4. Sediment Geotechnical Properties

[23] In independent tests we measured key properties of samples of the SG and SGM, including the maximum angles of repose for both basal and internal sliding of dry sediment, internal friction angles of water-saturated sediment subject to drained, uniaxial compression in triaxial cells, drained compression indices and secant Young's moduli (also measured in triaxial cells), saturated hydraulic conductivities as a function of porosity, wet bulk densities of deposits at the conclusion of experiments, and saturated hydraulic diffusivities (i.e., consolidation coefficients) inferred from various other measurements. Tables 2 and 3 summarize the results of this testing. Although many of the tests employed standard equipment and protocols, some were novel and merit further explanation, provided in Appendix C.

[24] Our most basic finding about sediment properties was that the angles of repose observed in tilt-table tests (with confining stresses ~2 kPa) were about 28° for smooth beds and 40° for rough beds, whereas internal friction angles were consistently close to 39° for both the SG and SGM. Thus, in our debris-flow experiments with rough beds, the static basal friction angle was essentially the same as the internal friction angle, but with smooth beds, it was about 11° smaller.

[25] The internal friction angle of 39° inferred from tilt-table tests was a few degrees larger than friction angles inferred from axial compression tests conducted at 55 kPa confining stress, despite the fact that these tests employed exceptionally large, six-inch and fifteen-inch diameter triaxial cells and complete grain-size distributions [*Major et al.*, 1997]. The triaxial tests necessarily involved confining stresses much larger than those typical of our experimental debris flows (~2 kPa), however, limiting their relevance. The differences in triaxial and tilt-table results were consistent with steepening of Coulomb strength envelopes commonly observed at very low confining stresses [e.g., *Alshibli et al.*, 2000; *Fannin et al.*, 2005], but we found no evidence of significant sediment cohesion.

[26] Our static and quasi-static measurements did not address evolution of debris properties in moving flows, but some insight to this evolution resulted from making measurements on deposits after flows came to rest. We found that water-saturated, fine-grained slurries constituting the core of most deposits had mean bulk densities of 2100 ± 110 kg/m^3 for the SGM and 2070 ± 90 kg/m^3 for the SG, which differed negligibly from the saturated bulk densities of sediment loaded behind the headgate (Table 2). On the other hand, we found that unsaturated, gravel-rich debris that invariably accumulated in levees at deposit margins had dry bulk densities of 1980 ± 190 kg/m^3, significantly larger than the initial dry bulk densities of sediment loaded behind the headgate. These high levee densities appeared to result

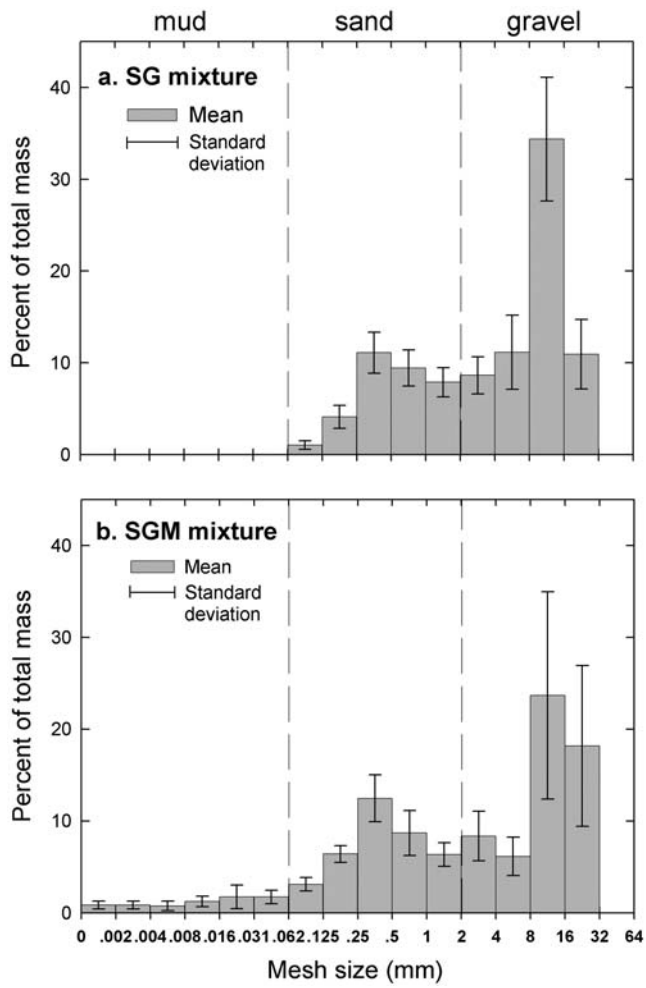

Figure 5. Grain-size distributions of the two sediment mixtures used in experiments. Histogram bars depict the mean in each size class and whiskers show ±1 standard deviation from the mean obtained from N analyses. (a) SG mixture, N = 20; (b) SGM mixture, N = 16.

Table 2. Sediment Volumetric and Water-Budget Data[a]

Property	Experiment Subset		
	SGM Rough Bed[b]	SG Rough Bed[b]	SG Smooth Bed[b]
Number of experiments in subset	8	9	11
Initial sediment volume behind headgate, including pore space (m^3)	9.73 ± 0.45 $N = 8$	9.80 ± 0.33 $N = 9$	9.72 ± 0.44 $N = 11$
Initial sediment water content, weight percent (water weight ÷ dry sediment weight) × 100	8.0 ± 2.8 $N = 27$	6.6 ± 2.0 $N = 27$	6.1 ± 1.5 $N = 21$
Net water added to sediment prior to flow release (m^3)	2.05 ± 0.29 $N = 8$	2.20 ± 0.52 $N = 9$	2.22 ± 0.31 $N = 11$
Total water (initial + added) in sediment at time of flow release (m^3)	3.34 ± 0.45 $N = 8$	3.30 ± 0.22 $N = 9$	3.17 ± 0.23 $N = 11$
Mean sediment porosity, before water application	0.39	0.37	0.36
Mean pore volume before/after 2% compaction caused by water application (m^3)	3.8/3.6	3.6/3.4	3.5/3.3
Mean saturation of pore space at flow release (%)	93	97	96
Mean wet bulk density of sediment at flow release (kg/m^3)	2010	2060	2070
Wet bulk density of slurry deposits after flow has ceased (kg/m^3)	2100 ± 110 $N = 3$	2070 ± 90 $N = 12$	2070 ± 90 $N = 12$

[a]Tabulated values indicate the mean ±1 standard deviation obtained from N measurements. Where N differs from the number of experiments in a subset, measurements were performed on multiple samples, each ~1000 cm^3. Where no N value or standard deviation is listed, tabulated values are not the result of direct measurements but instead represent mean values calculated using other data listed here or in Table 3.

[b]Dates of experiments included in analysis are, for SGM on rough bed, 9-28-2000, 9-13-2001, 9-12-2002, 9-17-2002, 6-19-2003, 6-25-2003, 9-22-2004, 9-23-2004; SG on rough bed, 9-19-2000, 9-21-2000, 9-25-2000, 9-26-2000, 9-18-2002, 9-19-2002, 6-17-2003, 6-24-2003, 9-20-2004; SG on smooth bed, 4-19-1994, 4-21-1994, 4-26-1995, 7-26-1995, 6-18-1996, 6-20-1996, 6-21-1996, 6-22-1996, 6-23-1996, 8-27-1996, 8-28-1996.

from imbrication of the bladed gravel clasts during deposition [cf. *Major*, 1998].

4. Experiment Description

[27] We initiated debris-flow motion in each experiment by using a hydraulic system to abruptly release the restraint on the side-hinged, two-piece steel headgate. This release, combined with the great static force of wet debris bearing against the gate (40–80 kN), caused it to swing open horizontally in about 1 s, reminiscent of the sudden opening of a saloon door when a miscreant is discharged. The resulting debris flows consequently began as nearly ideal dam-break flows, and departures from this ideal were due mostly to the evolving force distribution in the debris as it pushed against the opening gate.

[28] As the gate began to open, it exposed a vertical face of debris that initially underwent a trivial amount of forward

Table 3. Strength, Compression, and Hydraulic Properties of Sediment Samples[a]

Property	Experiment Subset		
	SGM Rough Bed	SG Rough Bed	SG Smooth Bed
Dry bulk density (kg/m^3)	1650 ± 107 $N = 22$	1710 ± 119 $N = 15$	1718 ± 68 $N = 10$
Basal friction angle (degrees) from maximum angle of repose in tilt-table tests	40.7 ± 2.1 $N = 12$	39.6 ± 1.1 $N = 7$	28.0 ± 0.8 $N = 8$
Internal friction angle (degrees) from maximum angle of repose in tilt-table tests	39.6 ± 2.7 $N = 14$	39.3 ± 3.0 $N = 20$	39.3 ± 3.0 $N = 20$
Internal friction angle (degrees) from triaxial compression in 6-inch cell	37 $N = 1$	39 $N = 1$	39 $N = 1$
Internal friction angle (degrees) from triaxial compression in 15-inch cell	33 $N = 1$	35 $N = 1$	35 $N = 1$
Saturated hydraulic permeability, k, (m^2) from constant-head permeameter tests with porosities ranging from 0.32 to 0.44	4×10^{-12} to 4×10^{-11} $N = 9$	1×10^{-11} to 5×10^{-10} $N = 12$	1×10^{-11} to 5×10^{-10} $N = 12$
Compression index, from axial loading in six-inch triaxial cells	0.09 $N = 1$	0.05 $N = 1$	0.05 $N = 1$
Secant Young's modulus, E, from axial strain in six-inch cells at 55 kPa confinement (Pa)	5×10^6 $N = 1$	5×10^6 $N = 1$	5×10^6 $N = 1$
Soil saturated hydraulic diffusivity, D, minimum calculated from kE/μ[b] (m^2/s)	2×10^{-2}	5×10^{-2}	5×10^{-2}
Slurry saturated hydraulic diffusivity, D, from slurry consolidation tank or flume deposit consolidation measurements[c] (m^2/s)	1×10^{-6} to 3×10^{-6} $N = 6$	10^{-4} $N = 2$	10^{-4} $N = 2$

[a]Tabulated values indicate the mean ±1 standard deviation obtained from N measurements.

[b]Calculation of D assumes that pore fluid viscosity is that of water alone: $\mu = 0.001$ Pa-s.

[c]Slurry consolidation measurements are described by *Major* [2000].

Figure 6. Photographs of an SG debris flow discharging through opening headgate. The "t" denotes approximate time elapsed since gate began to open. White material visible at flow front and on flume bed is polyurethane foam used to seal gate and catch leaks. A transverse shadow is cast by a crossbeam suspending a laser at $x = 2$ m.

toppling, followed by pervasive downward settlement and down-flume extension of the leading edge of the debris (Figure 6). Trailing debris mobilized progressively over the course of 2 to 3 s as a displacement front propagated from the opening gate into the static mass upslope. Although this front propagation broadly mimicked that observed in dam-break flows of liquids [cf. *Ancey et al.*, 2008], it was typically accompanied by development of transverse surface fissures like those observed in failing earth embankments and slopes. When the displacement front reached the upper edge of the static debris, it released a small (~0.1 m^3) pond of water that accumulated there during water application. The ponded water was then engulfed by adjacent sediment, creating a tail of dilute debris that was the last to evacuate the headgate area.

[29] Nearly all of the debris typically passed the headgate within 5 s of the gate release, but the tail of the flow was commonly deflected toward the flume centerline by the headgate doors when they rebounded following impact with rubber shock absorption bumpers. This deflection was perhaps the least reproducible aspect of debris-flow initiation in our experiments, but it had no obvious effect on most of the debris.

[30] In our earliest experiments we placed tethered electronic pressure transducers in the debris loaded behind the headgate to monitor pore pressure changes during gate opening. As in landslide experiments with similarly wet, loosely packed soils [*Iverson and LaHusen*, 1989; *Reid et al.*, 1997; *Iverson et al.*, 2000], we found that pore pressures increased dramatically as movement commenced, typically doubling from hydrostatic values to near-lithostatic values within ~1 s after the headgate opened. We inferred that our experimental debris flows invariably commenced motion in a nearly liquefied state, and we subsequently discontinued pore pressure monitoring behind the headgate to focus on data collection downslope.

[31] During the first ~3 s of motion, the debris flows elongated markedly, but their surfaces retained some visible structure (e.g., relative positions of clasts) inherited from the initial, static debris. At the same time, coarse-grained snouts developed as a result of migration of surface grains toward the flow fronts and preferential retention of coarse clasts there. After about 3–4 s (~30 m) of downslope motion, flow snouts appeared to consist mostly of gravel, whereas debris trailing the snouts appeared distinctly finer and wetter. Agitation of this wet debris eventually eliminated visible remnants of structure inherited from the initial state.

[32] As the gravelly flow snouts advanced downslope, a smaller volume of gravel saltated ahead. In some instances, isolated saltating clasts were followed by clouds of saltating gravel that made visual discrimination of the positions of debris-flow snouts quite difficult. (As a rule, we could identify snout positions most precisely on the basis of sensor data, as described below.) When debris-flow snouts were observable, however, they exhibited a form of wave breaking in which clasts reaching the crests of snouts tumbled down their forward faces, slowed when they contacted the bed, and were overridden. Therefore, although snouts acted to some extent as moving dams that impounded trailing, more-fluid debris, the sediment constituting the dams evolved continuously.

[33] In every experiment, prominent secondary waves appeared spontaneously on the surface of the debris flows, generally within the first ~30 m of downslope motion, and they divided each flow into a series of about 5 to 20 surges with diverse amplitudes, speeds, and periods. We adopt "roll wave" as a descriptive term for these surges, although the mechanics of instability and wave propagation in the debris probably differed significantly from those in water [*Schonfeld*, 1996; *Zanuttigh and Lamberti*, 2007]. Indeed, formation and growth of the debris-flow roll waves appeared intimately linked to the process of grain-size segregation. Randomly distributed concentrations of gravel appeared to exert more flow resistance than did surrounding debris, and as gravel collected in these resistive patches, their growth eventually produced discernible wavefronts with gravelly snouts. As the waves grew in amplitude and width, finer-grained debris that accumulated behind them helped push them forward. With the benefit of this added thrust, larger waves commonly overtook and cannibalized smaller ones.

[34] The presence of gravelly snouts in both debris-flow fronts and roll waves affected flow runout and deposition, owing largely to the process of lateral levee formation. As gravelly snouts reached the base of the flume, they began to decelerate; then, more-fluid, finer debris behind the snouts shouldered aside the gravel, leaving gravel-rich lateral levees in its wake. In some cases levee formation began several

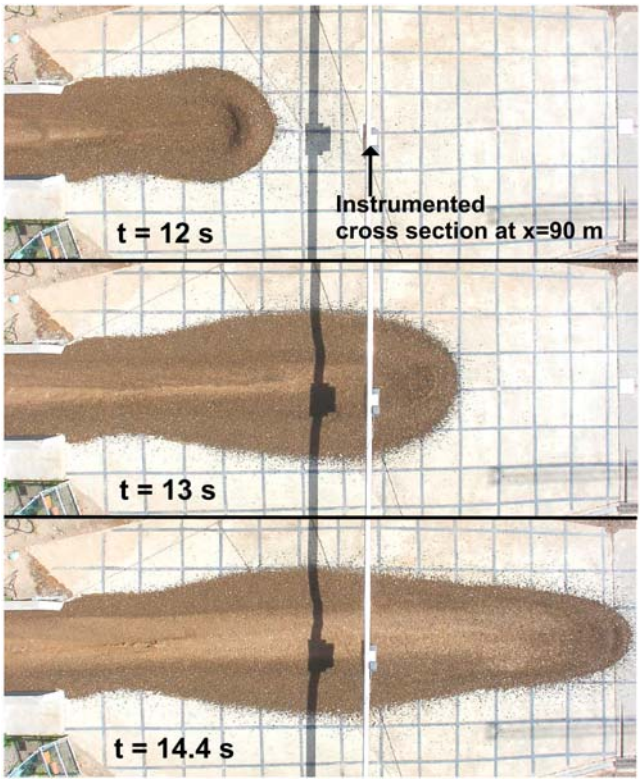

Figure 7. Vertical aerial photographs of a SGM debris flow crossing runout pad. A 1-m grid on pad provides scale. The "t" denotes approximate time elapsed since headgate began to open. Dark-toned debris consists predominantly of gravel. Light-toned material consists predominantly of water-saturated muddy debris. A transverse shadow is cast by a crossbeam suspending a laser at x = 90 m.

meters before flows reached the flume mouth, but in all cases it was most pronounced where flows issued from the flume and began crossing the unconfined runout surface (Figure 7). Levee formation generally persisted as long as successive gravelly fronts crossed the runout surface, and it produced deposits bounded mostly by lateral levees and in some cases by multiple generations of nested levees deposited by successive roll waves.

[35] Evidence of gravelly snouts was more poorly preserved at the distal margins of deposits, where snouts as well as parts of lateral levees were commonly overridden by trailing, fine-grained debris. Swamping of deposits by this watery debris obscured many structural and stratigraphic relationships, and as a consequence, depositional processes could be interpreted accurately only by combining deposit mapping, dissection, and sampling with study of run-time videotapes and photographs [e.g., *Major*, 1996, 1997, 1998; *Major and Iverson*, 1999].

5. Measurement Methods

5.1. Photography, Videography, and Flow-Front Tracking

[36] In each experiment we deployed 3–5 still-frame cameras and 6–8 video cameras to record views that included full-flume perspectives, close-up perspectives, and vertical aerial perspectives of the runout area at the base of the flume. We synchronized our videotape recordings with electronic sensor data through use of a gate-open detection circuit described below. We subsequently distilled the recordings and converted them into digital video files [*Logan and Iverson*, 2007].

[37] We tracked flow-front positions by playing videotapes frame by frame and recording the times at which the fronts reached reference stripes painted at 5-m intervals on the flume bed. Because standard NTSC videotapes advance at a nominal rate of 30 frames per second, the time resolution of this procedure was about 0.03 s. The spatial resolution varied with camera position and video format, but was consistently better than 0.5 m at each 5 m interval. (As technology evolved from 1994 to 2004, we upgraded our collection of video cameras from VHS to Hi-8 and then to digital formats. As a consequence, the resolution of our recordings improved with time.)

[38] Our still-photo sequences provided image resolution superior to that of video recordings, but lacked precise synchronization with the gate-open time. Like video technology, still-photo technology evolved during the eleven-year period in which our experiments were conducted, resulting in our gradual transition from analog to digital photography.

5.2. Electronic Sensors

[39] A chief objective in our experiments was measurement of the evolving flow thickness normal to the bed, h, basal total normal stress, σ_{bed}, and basal pore fluid pressure, p_{bed}, as debris flows moved downslope and formed deposits. We made such measurements electronically at three cross sections, nominally located at x = 32 m, x = 66 m, and x = 90 m. At the two upper cross sections we typically used multiple, closely clustered sensors deployed along the flume centerline, where instrumentation ports were built into the flume bed. At a nominal x = 32 m, three centerline ports were located at x = 31.7 m, 32.3 m, and x = 32.9 m. At a nominal x = 66 m, the three ports were at x = 65.6 m, x = 66.2 m and x = 66.8 m. In the runout area at the base of the flume, a single port nominally located at x = 90 m was positioned precisely at x = 89.9 m. At all of these locations our stress and pore pressure sensors were installed so that measurements were made on surfaces flush with the flume bed, and laser flow-thickness sensors were installed on crossbeams mounted above the bed (Figure 8).

[40] Our systems for measuring basal normal stress consisted of Omega Model LC (or equivalent) S-beam load cells with their bases mounted to stiff steel undercarriages and their tops mounted to half-inch thick, circular steel plates with an area of 500 cm^2. (In experiments prior to 1997, we substituted 22 cm^2 plates for the 500 cm^2 plates at x = 32 m, but in every case the configuration was similar to that illustrated in Figure 8.) We sealed the margins of the plates with soft gaskets that prevented sediment from intruding and jamming but added negligible mechanical stiffness to the system. When subjected to controlled, impulsive loading, these stress-measurement systems exhibited in situ natural frequencies ranging from 110 to 160 Hz. (Any use of trade, product, or firm names is for descriptive purposes only and does not imply endorsement by the U.S. government.)

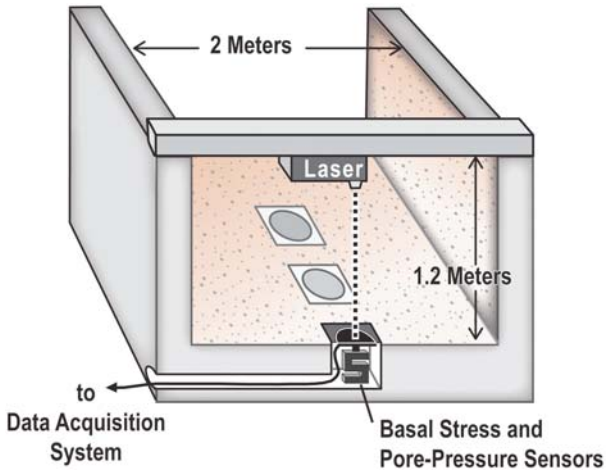

Figure 8. Schematic cutaway view of instrumented flume cross section.

[41] During calibrations of our stress-measurement systems with static weights, linearity of the sensor responses was generally excellent ($r^2 > 0.99$), and repeatability of regression line slopes was within a few percent. The least reproducible aspect of sensor performance was the output observed with no weight applied. This zero value commonly drifted from day to day and sometimes even hour to hour, possibly in response to changes in temperature and humidity. As a result, we determined zero values not from calibration lines but instead from the sensor outputs recorded a few seconds prior to debris-flow arrival. With this approach, our calibrations indicated that we could confidently measure normal stresses with an accuracy of about ±0.1 kPa.

[42] Our systems for basal pore pressure measurement used Honeywell Microswitch differential strain-gage pressure transducers (model 26PCCFA3D, 0–15 psi) vented to the atmosphere and mounted so that each transducer diaphragm was separated from passing debris by a ~0.5 cm^3 water-filled cavity. We covered this cavity with a sintered, tinned brass filter of the type sometimes used on scuba pressure regulators, an arrangement that permitted direct pressure communication between pore water and the transducer diaphragm without exposing the diaphragm to sand and coarser sediment. (Conventional ceramic filters were unsatisfactory for this purpose, because they drastically attenuated pressure fluctuations at frequencies greater than a few Hz.) Our pressure-measurement systems generally performed well, although the filters sometimes plugged with mud during the waning stages of flow, making the sensors unresponsive and necessitating disassembly and cleaning between experiments. In most cases we deployed several pore pressure sensors at individual measurement cross sections, and we discarded data from sensors that clearly became plugged.

[43] Calibrations of our pore pressure sensors using static water pressures yielded regression line slopes that were both linear ($r^2 > 0.99$) and reproducible. Like the normal-stress sensors, however, the pore pressure sensors exhibited some zero drift, and we consequently determined zeros for use in data processing from values recorded just prior to debris-flow arrival in each experiment. With this approach, our calibrations indicated that we could reliably measure basal pore fluid pressures with an accuracy of about ±0.05 kPa.

[44] We measured flow thicknesses normal to the slope at x = 32, 66, and 90 m using infrared laser triangulation sensors (Figure 8). These systems (Selcom optocator model 2008 or prior equivalent) resolved thickness variations ~1 mm at frequencies as high as 2000 Hz. Moreover, repeated calibrations of the lasers were remarkably stable and insensitive to environmental factors. The most significant limitation of the laser triangulation systems was the small surface area they sampled (<1 cm^2).

[45] From 1994 to 1996 we also made electronic flow-thickness measurements at x = 2 m, just downslope from the flume headgate. These measurements were problematic, however, because thickness variability at this location commonly exceeded 0.6 m, and our lasers were incapable of measuring over such a wide range. An ultrasonic transceiver we used as a substitute sometimes produced spurious output, and after repeated trials, we eventually devised a new type of laser system to replace the ultrasonic sensor. Here we present only the ultrasonic sensor data collected at x = 2 m during 11 experiments from 1994 to 1996.

5.3. Digital Data Acquisition

[46] Details of our data acquisition system evolved as technological advances enabled improvements, but in all cases, electronic sensor outputs were amplified near their sources, transmitted via shielded cables to a sheltered station near the base of the flume, and sampled digitally using a personal computer equipped with a 12-bit data acquisition card configured to record from 16 to 24 inputs at frequencies of either 500 or 2000 Hz per channel. Generally we performed no analog filtering of sensor output unless significant electronic noise was detected prior to an experiment. In such cases we reduced the noise by installing RC low-pass filters with RC = 0.005 s and a consequent half-power roll-off frequency of 32 Hz.

[47] In each experiment we dedicated one data acquisition channel to time registration. This channel recorded the voltage of an electrical circuit that was broken when the flume headgate began to open. The resulting gate-open signal established the origin of the time coordinate used in all of our data processing and plotting. It also triggered electronic time-stamping of videotapes, thereby synchronizing the sensor data and video recordings.

5.4. Digital Data Processing

[48] Following data acquisition and conversion of electronic units to physical units, we manually reviewed graphs of the data and, in some cases, averaged the output from same-type sensors installed in close proximity to one another. For example, if all four pore pressure sensors at an individual cross section resisted plugging, we averaged the data from all to obtain a representative pore pressure time series for that cross section. Use of data from sensors in neighboring ports required insertion of small time shifts to account for small differences in flow-front arrival times. For example, if a flow traveled at ~10 m/s as it moved from x = 66.2 to 66.8 m, we inserted a time shift of 0.06 s before

averaging pore pressures measured at 66.2 m with those measured at 66.8 m.

[49] The next step in data processing was low-pass filtering to prepare the data from multiple experiments for aggregation. Although the raw data contained information with diverse wavelengths, ranging from the grain size to the flow size [*Iverson*, 1997], superposition of multiple time series degraded short-wavelength information into noise. Therefore, we focused on continuum-scale information with wavelengths larger than the characteristic flow thickness (~0.2 m), and we filtered the data accordingly. We employed a digital low-pass filter mimicking an RC analog filter with RC = 0.0053 s (implying a half-power roll-off frequency of 30 Hz), and we implemented this filter using a recursive algorithm in the time domain [*Bendat and Piersol*, 1986, p. 367]. Filtering visibly smoothed the data, but it preserved evidence of every roll wave we noticed during inspection of videotapes, and it yielded data with well-defined attenuation spectra. At frequencies less than about 10 Hz, attenuation was essentially zero. At higher frequencies, filtering caused the relative power (square of the gain) of the signal to attenuate progressively until it was diminished by about 75 percent at 50 Hz and by more than 90 percent at 100 Hz.

[50] After filtering, we decimated the data by re-sampling at a frequency of 100 Hz. This decimation facilitated computation of aggregated time series means and standard deviations at uniform intervals of 0.01 s, and it implied an effective Nyquist frequency of 50 Hz. Thus, at frequencies above 50 Hz, the decimated data retained small, remnant fluctuations representing noise associated with mechanical processes not sampled adequately at 100 Hz.

[51] Another key step in data processing involved time shifting aimed at preserving the sharpness of flow fronts when data from multiple experiments were averaged. Because not all flow fronts in any subset of 8 to 11 experiments arrived at a given measurement cross section at the same time, flow-front data became smeared during averaging if such time shifts were not applied. We used data from basal normal-stress sensors to establish flow-front arrival times with a precision of 0.01 s at each cross section in each experiment. (Laser data were less useful for determining arrival times, because the lasers commonly detected gravel that bounced ahead of flow fronts.) We then used the individual arrival times to compute a mean arrival time for each cross section in each set of experiments, and finally determined the desired time shifts by differencing the individual arrival times from this mean time. Time shifts determined in this way were generally less than 1 s.

[52] The last step in computing aggregated time series for each subset of 8 to 11 experiments was straightforward. Using the filtered, decimated, time-shifted data, we computed means and sample standard deviations of the calibrated output of each sensor for each 0.01 s interval in each experiment subset.

[53] A different type of data processing was necessary to document the amplitudes of roll waves we observed in individual debris flows. Unlike roll waves in classical fluid-mechanics experiments, roll waves superposed on the highly unsteady flows in our experiments could not be identified by separating repetitive fluctuations in thickness, h, from a background of constant h. Indeed, preliminary analyses of our laser data showed that the time series $h(t)$ generally had power spectra similar to those of fractional Brownian noise, implying that fluctuations of h had a high degree of scale invariance [*Turcotte*, 1992]. To identify significant waves within this fluctuating background, we first used the filtered, decimated, 100-Hz data described above to compute a 100-point moving median of $h(t)$ for each experiment, and thereby generated a smoothed time series $\overline{h}(t)$ without scale-dependent bias [*Press et al.*, 1986, p. 497]. We then computed the residuals $h(t) - \overline{h}(t)$ and tabulated all residuals exceeding 0.02 m as roll waves. We used this 0.02 m cutoff in order to focus on fluctuations with amplitudes greater than the diameters of the larger individual clasts in the flows. Similarly, we used filtered, decimated data in the computations in order to focus on features with wavelengths greater than about 0.2 m.

5.5. Deposit Mapping

[54] We mapped the morphology of deposits formed at the base of the flume using several techniques. Typically, we created deposit isopach maps by first making topographic maps of the deposit surfaces and then subtracting the topography of the underlying concrete runout pad (Figure 3b). From 1994 to 2000, we used a total-station theodolite to survey about 100 elevations of points on the surface of each deposit, which served as a basis for constructing topographic contours either by a hand or by computational interpolation. In 2001–2004 we used different mapping techniques that employed either laser leveling to establish deposit topography or a dipstick to measure deposit thicknesses at 1-m or finer intervals. When we employed laser leveling, we used a paste extrusion device to place analog contour lines directly on the deposit, then photographed the contoured deposit from overhead and rectified the photos digitally to obtain analog topographic maps [*Iverson*, 2003].

6. Measurement Results

6.1. Flow-Front Positions and Speeds

[55] We tracked the position of each flow front as far as possible - until it stopped, ran out of the field of view of our most distal video camera, or encountered an obstruction (intentionally placed in the flow path in some experiments). With these limitations, we measured the positions of all fronts as far as x = 70 m, and some as far as x = 100 m, as summarized in Figure 9. The most important features in Figure 9 are the traces denoting mean flow-front positions for each subset of experiments: SGM rough bed, SG rough bed, and SG smooth bed. We were able to compute these means only as far as x = 70 or 75 m, but they nevertheless demonstrate clear similarities and differences between subsets.

[56] For each experiment subset, marked flow-front acceleration typically lasted only until about t = 2 s, followed by front propagation at nearly constant speeds from about t = 2 to 6 s. (Figure 9). During this 4 s interval, flow-front speeds on the rough bed averaged about 10 m/s for both the SGM (Figure 9a) and SG (Figure 9b), whereas speeds averaged about 13 m/s for the SG flows on the smooth bed (Figure 9c).

[57] After $t \approx 6$ s, differences between the mean flow-front behaviors in the three experiment subsets became more conspicuous. The SGM rough-bed flow fronts typically reached x = 70 m about 1.5 s before the fronts in SG rough-

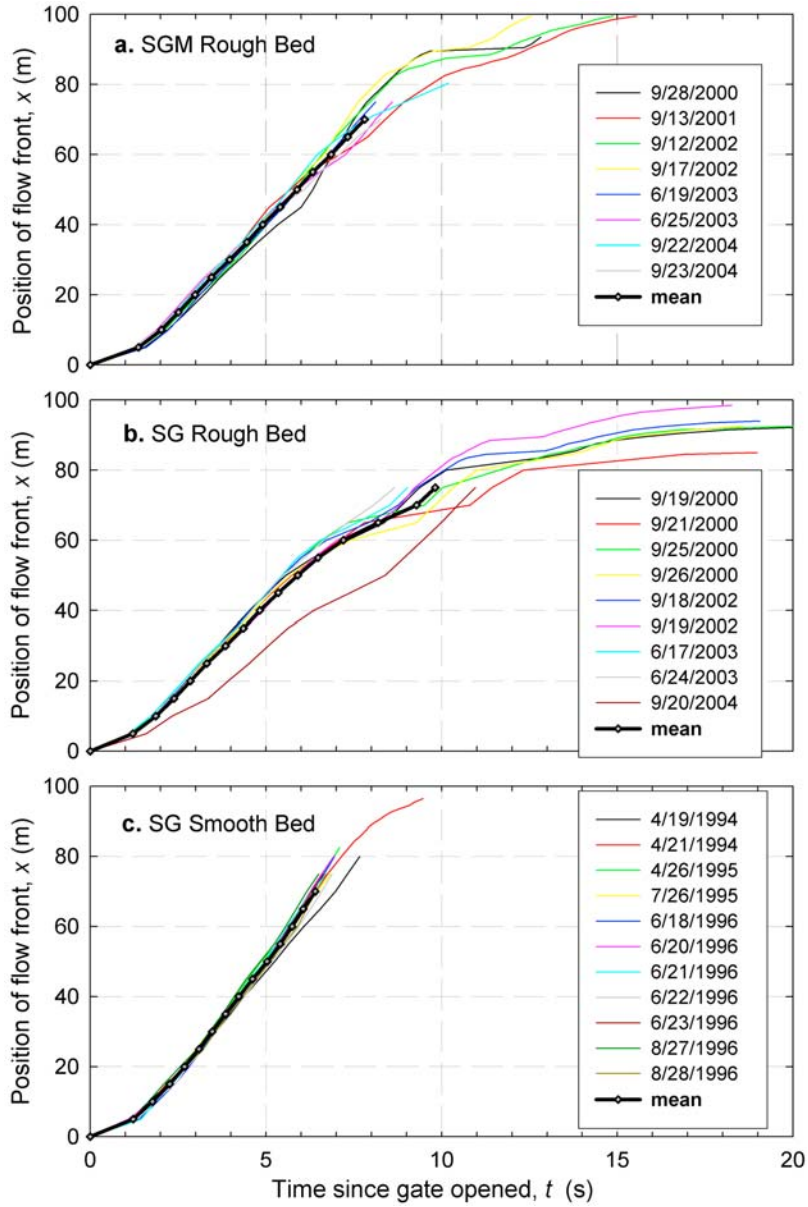

Figure 9. Position of flow fronts as a function of time. Colored traces depict behavior measured in individual experiments. Black lines depict mean behavior calculated for each of the three experiment subsets, and data points depict calculated mean values at 5-m increments. (a) SGM Rough bed; (b) SG Rough bed; and (c) SG Smooth bed.

bed experiments but about 1.4 s after the fronts in SG smooth-bed experiments (Figure 9). Deceleration of SGM rough-bed fronts and SG smooth-bed fronts did not begin until flows encountered the break in slope at x = 74 m, but deceleration of SG rough-bed fronts typically began at about x = 55 m (Figure 9b). This deceleration resulted from a tendency of gravel-rich flow fronts to come nearly to rest at about x = 55 to 60 m until they were overtaken by trailing surges of wetter, fine-grained debris. Similar stalling of fronts did not occur in SGM flows on the rough bed because nearly liquefied, trailing debris pushed against the flow fronts continually.

6.2. Times Series of h at x = 2 m

[58] In the 11 experiments conducted from 1994 to 1996, we collected ultrasonic sensor data sufficient to compute means and standard deviations of evolving flow thicknesses at x = 2 m. The means show that along the flume centerline, flow fronts typically reached x = 2 m at about t = 0.9 s (Figure 10). The subsequent peak in flow thickness ($h \approx 0.6$ m) occurred at about t = 1.9 s, indicating a steep rising stage. The falling stage was more gradual, but when h approached 0 at $t \approx 4$ s, the sensor commonly yielded spurious negative h values. As a consequence, we regard Figure 10 as a reliable depiction of flow thickness at x = 2 m only up to t = 4 s.

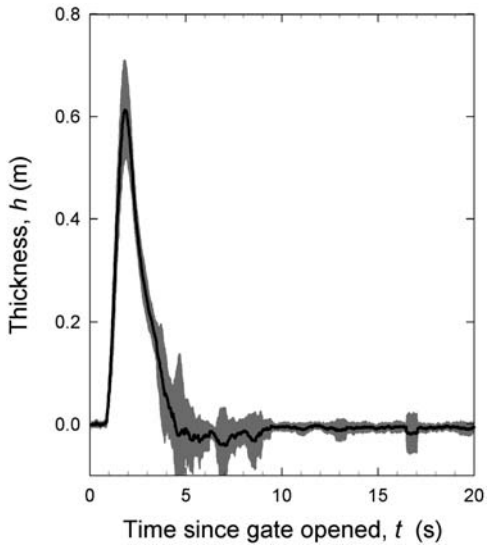

Figure 10. Mean (black line) and standard deviation (gray shaded area) of flow thicknesses measured at x = 2 m.

We believe this depiction is representative of all of our experiments, however (not only of those from 1994 to 1996), because every experiment involved the same sediment preparation and flow-release protocols, every flow moved across a smooth bed from x = 0 to 6 m, and every videotape documented consistent behavior as the headgate opened.

6.3. Rough-Bed Time Series of h, σ_{bed}, and p_{bed} at x = 32, 66, and 90 m

[59] Our most comprehensive data sets summarize aggregated sensor measurements made at x = 32, 66, and 90 m in SGM and SG experiments with rough beds. In graphs that depict time series of h, σ_{bed}, and p_{bed} at these cross sections (Figures 11–13), we employ axes for flow thickness, h (measured in m) scaled 20 times larger than the axes for basal total normal stress, σ_{bed}, and basal pore fluid pressure, p_{bed} (each measured in kPa). This choice of scales facilitates comparison of h, σ_{bed} and p_{bed} because it results in a perfect superposition of all three time series if an ideal, liquefied state exists in which $\sigma_{bed} = p_{bed} = \rho g h$ and ρ = 2040 kg/m^3. (In choosing our graph scales we avoided use of the more precise formula $\sigma_{bed} = p_{bed} = \rho g h \cos\theta$, because this formula would have necessitated use of different scaling factors for cross sections with different slopes.)

[60] The means and standard deviations of h, σ_{bed} and p_{bed} for the SGM and SG flows on rough beds have many features in common (Figures 11 and 12), despite the fact that the SGM flows reached x = 66 m and 90 m well ahead of the SG flows. In both types of flows the long-period waveforms characterizing flow-passage at x = 32 and 66 m have mean durations ~10 s, mean peak h values ~0.2 m, and h standard deviations ~0.05 m at most times (Figures 11a and 11b, and 12a and 12b). For both types of flows the mean waveforms at x = 90 m differ from those at x = 32 and 66 m by virtue of their briefer peaks and terminations in plateaus (Figures 11c and 12c). Thus, for both SGM and SG flows, the aggregated h data imply that motion between x = 32 and 66 m grossly

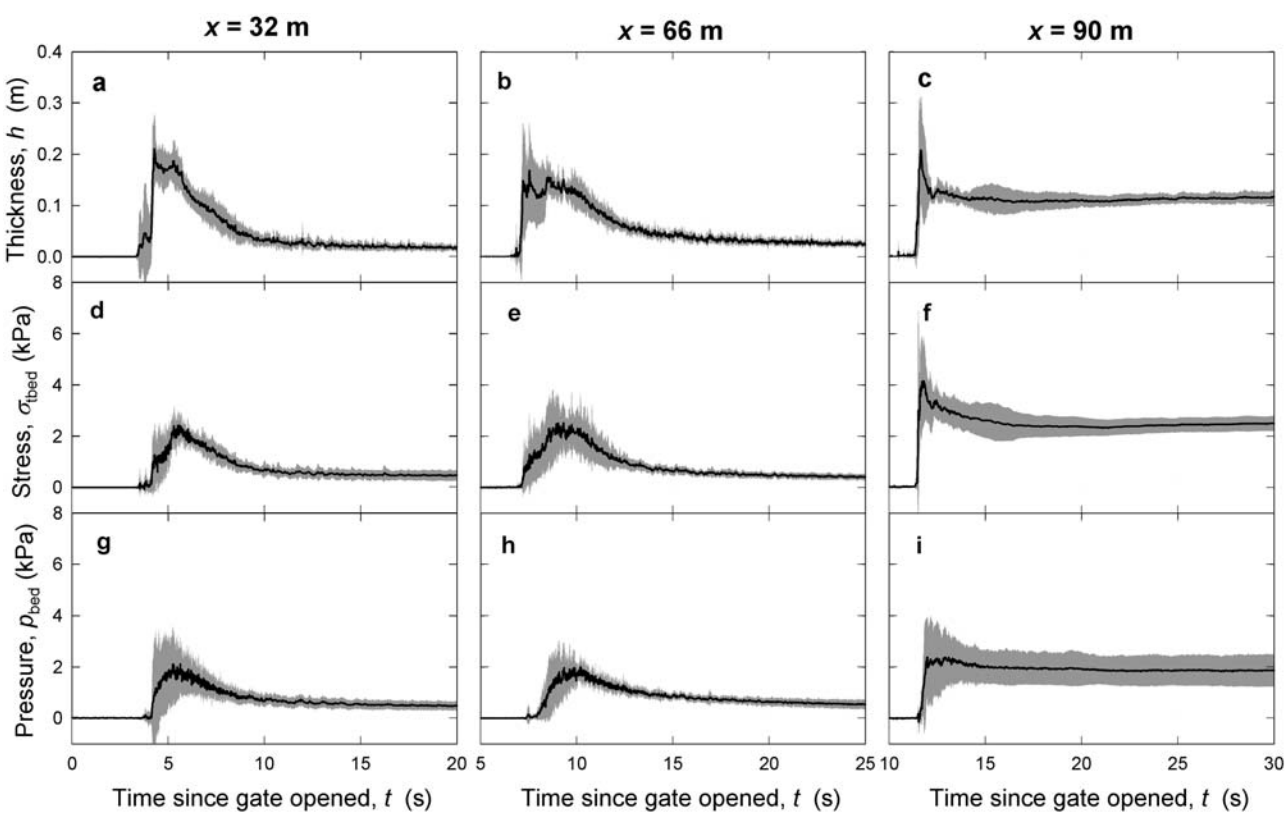

Figure 11. Aggregated time series data for SGM rough-bed experiments. Mean values (black lines) and standard deviations (gray shaded areas) are shown.

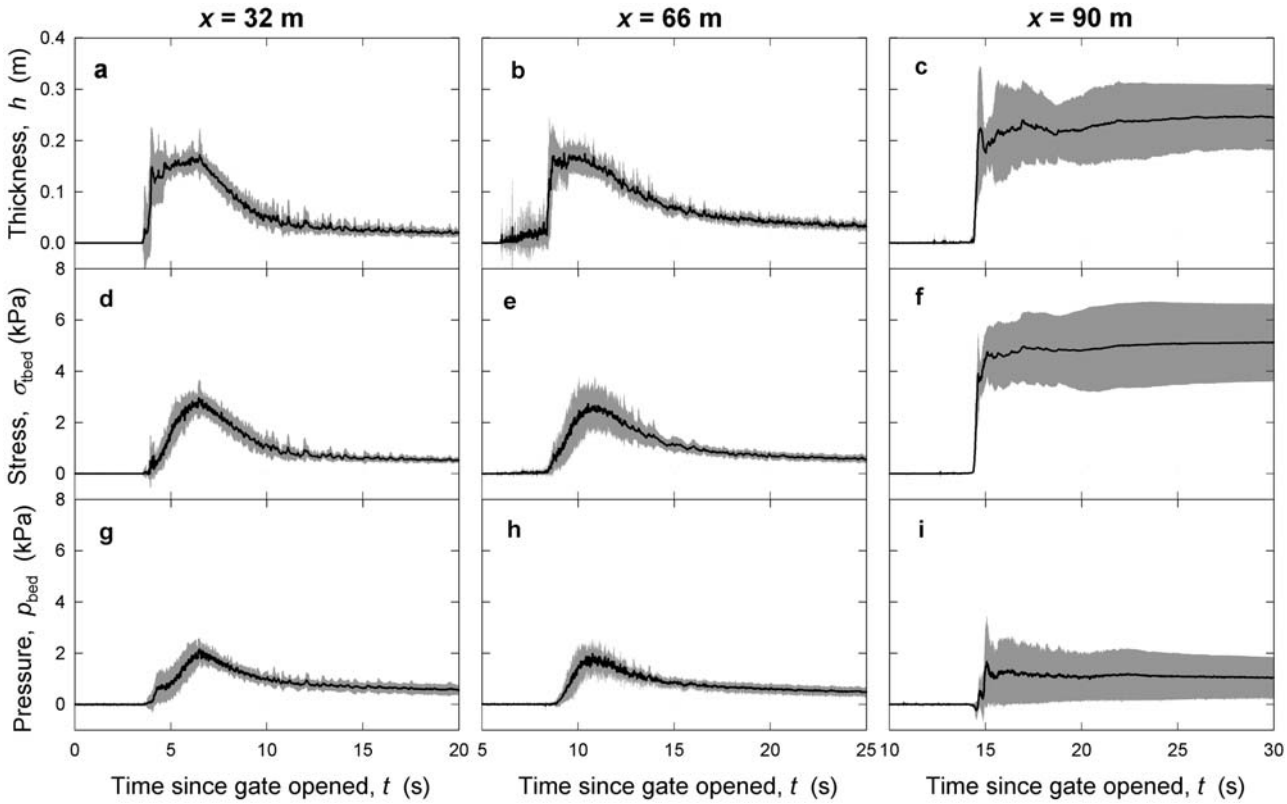

Figure 12. Aggregated time series data for SG rough-bed experiments. Mean values (black lines) and standard deviations (gray shaded areas) are shown.

involved downslope translation of a fixed waveform (considerably flatter and longer than the waveform at $x = 2$), and that waveform compression occurred when flows encountered reduced slopes and ultimately formed deposits at $x = 90$ m. (In Figures 11–13 the data for $x = 90$ m come from subsets of four experiments: SGM 9-28-2000, 9-13-2001, 9-12-2002, 9-17-2002; and SG 9-25-2000, 9-26-2000, 9-18-2002, 9-19-2002; because in the other rough-bed experiments we modified the boundary conditions in the runout area.)

[61] Relationships between σ_{bed} and p_{bed} reveal complications not apparent in the h data, however (Figures 11d–11i and 12d–12i). Although the time series for h, σ_{bed}, and p_{bed} typically superpose more or less as predicted by the idealization $\sigma_{bed} = p_{bed} = \rho g h$ with $\rho = 2040$ kg/m^3, departures from this ideal are significant (outside the 1 standard deviation envelope) at $x = 32$ and 66 m, particularly during the first few seconds of flow-front passage. The departures are partly attributable to the effect of slope alone (with $\theta = 31°$, a steadily flowing liquefied mass with uniform h obeys $\sigma_{bed} = p_{bed} = \rho g h \cos 31° = 0.857\ \rho g h$), but the factor 0.857 is insufficient to explain the departure timing and magnitude.

[62] We highlight the magnitude and timing of changes in h, σ_{bed}, and p_{bed} for the SGM and SG flows by juxtaposing the mean time series for both types of flows on common axes with an expanded time scale (Figure 13). In both the SGM and SG flows, the mean arrival of the flow front at $x = 32$ m at about $t = 4$ s is marked by concurrent increases in h, σ_{bed}, and p_{bed} (Figures 13a and 13d). For roughly 1 s thereafter, however, the values of σ_{bed} and p_{bed} are less than half those expected from $\sigma_{bed} = p_{bed} = 0.857\ \rho g h$, and such disproportionately small σ_{bed} and p_{bed} values persist in flow fronts at $x = 66$ m for both SGM and SG (Figures 13b and 13e). Thus, in both types of flows, flow fronts are apparently highly dilated and unsaturated at $x = 32$ and 66 m, an inference we address further in the section on Implications for Modeling below.

[63] Evolution of σ_{bed} and p_{bed} at $x = 32$ m provides evidence that a liquefied or partly liquefied basal debris layer may coexist with a dilated flow-front surface, but that after front passage, liquefied debris encompasses the entire flow thickness. In SGM flows the liquefaction condition $p_{bed} \approx \sigma_{bed}$ is always maintained, but both σ_{bed} and p_{bed} are much smaller than $0.857\ \rho g h$ at the flow front (Figure 13a). Both σ_{bed} and p_{bed} subsequently increase, however, until $\sigma_{bed} = p_{bed} = 0.857\ \rho g h$ applies almost exactly. Analogous behavior occurs in the SG flows at $x = 32$ m, except in these flows $p_{bed} \approx 0.6\ \sigma_{bed}$ applies during passage of the dilated front (Figure 13d).

[64] For both the SGM and SG flows, the mean flow-front behavior measured at $x = 66$ m is similar to that measured at $x = 32$ m, with one important exception: following front passage at $x = 66$ m, the increase in p_{bed} lags behind that of σ_{bed} by about 1 s, implying the existence of a ~10 m long surge front entirely lacking positive pore fluid pressure (Figures 13b and 13e). Subsequently, p_{bed} gradually increases relative to σ_{bed}, so that within about 2 s the idealization $\sigma_{bed} = p_{bed} = 0.857\ \rho g h$ again applies in the SGM flows, and $p_{bed} \approx 0.6\ \sigma_{bed}$ again applies in the SG flows.

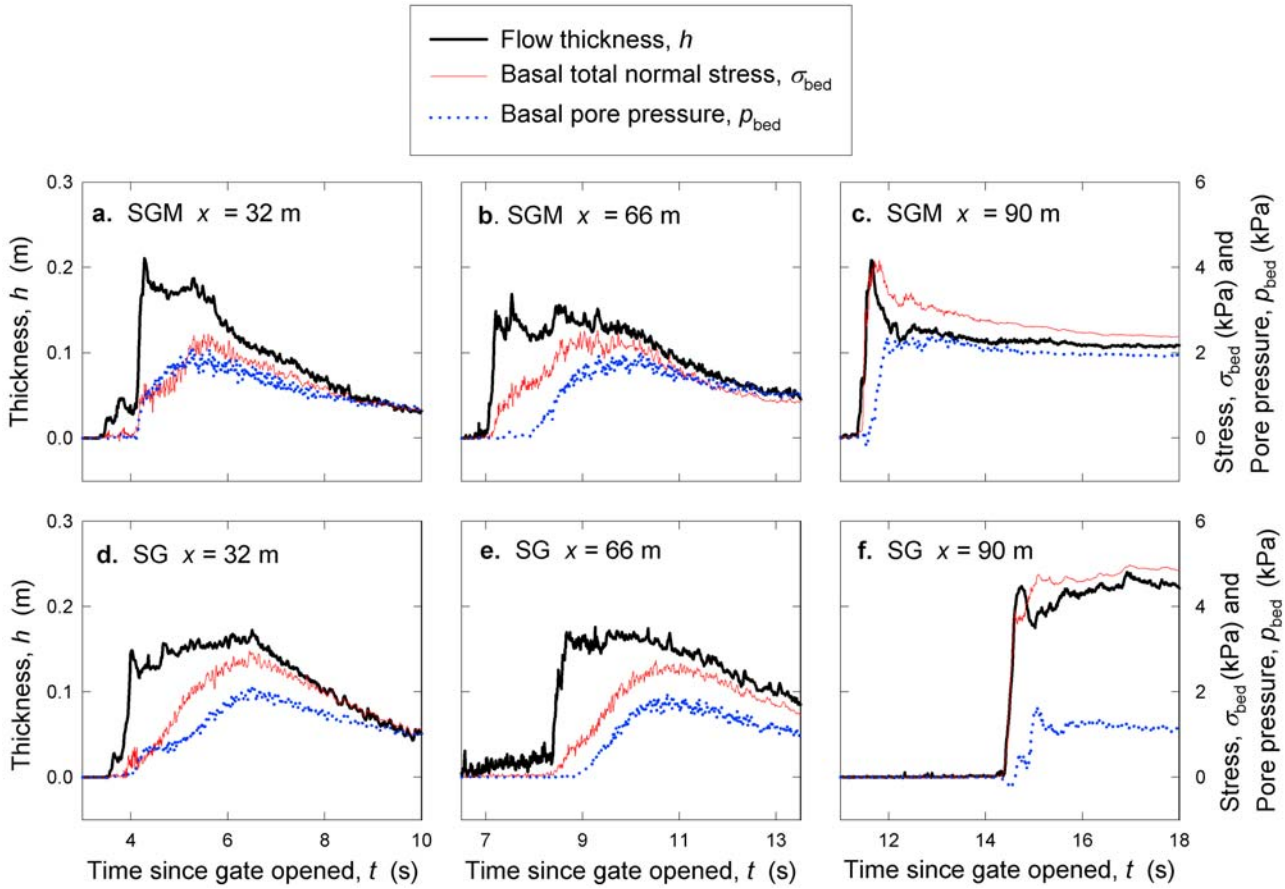

Figure 13. Juxtaposed mean values of aggregated time series data for flow fronts. (a–c) SGM rough-bed experiments; (d–f) SG rough-bed experiments.

[65] In contrast to the behavior measured at x = 32 and 66 m, at x = 90 m the mean time series of σ_{bed} mimics the mean time series of h almost exactly in both the SGM and SG flows, even during passage of the flow front (Figures 13c and 13f). Thus, in the gently sloping runout area at the base of the flume, there is little evidence of flow-front dilation. Moreover, the lag between the rise of σ_{bed} and p_{bed} during front passage is reduced from about 1 s at x = 66 m to about 0.5 s at x = 90 m in both the SGM and SG flows (Figure 13). This lag reduction is commensurate with observations of longitudinal compression of the flow front as it decelerates (Figure 7). The strikingly consistent flow-front behavior in SG and SGM flows at x = 90 m occurs despite the fact that the SG flows typically have front arrivals about 30 percent slower, and values of h and σ_{bed} about 100 percent larger, than those of SGM flows (Figures 11c and 12c).

[66] Following flow-front passage at x = 90 m, values of basal pore fluid pressure differ significantly in the SGM and SG flows. In the SGM flows the idealization $\sigma_{bed} = p_{bed} = \rho g h$ with ρ = 2040 kg/m^3 applies quite consistently after $t \approx$ 12 s, implying that debris that trails the flow front and forms a deposit at the sensor location is fully liquefied (Figure 13c). In SG flows a better approximation after flow-front passage is $p_{bed} \approx (1/4)\sigma_{bed}$, implying that the debris at x = 90 m is not fully saturated with liquid.

6.4. Smooth-Bed Time Series of h, σ_{bed}, and p_{bed} at x = 32 and 66 m

[67] Relationships between h, σ_{bed}, and p_{bed} measured at x = 32 and 66m for SG flows on smooth beds contrast markedly with the relationships summarized above for flows on rough beds. (For smooth-bed experiments we lack sufficient data from x = 90 m to compute aggregated time series, but *Major and Iverson* [1999] present some individual time series for that cross section.) Like the rough-bed time series in Figures 11 and 12, the aggregated smooth-bed time series show evidence of dilated flow fronts and near-liquefied flow bodies with $p_{bed} \approx \sigma_{bed}$, but they also show disproportionately large values of σ_{bed} and p_{bed} relative to values of h (Figure 14). Indeed, at x = 32 m, both σ_{bed} and p_{bed} average nearly three times larger than the idealized value $\sigma_{bed} = p_{bed} = \rho g h$ with ρ = 2040 kg/m^3, and at x = 66 m, both quantities average about two times larger than this idealized value. In absolute terms, the departures of the measured σ_{bed} and p_{bed} values from their idealized values are as much as 8 kPa, and they consistently fall outside the ±1 standard deviation envelopes of expectations based on values of h (Figure 14).

[68] The anomalously large values of σ_{bed} and p_{bed} appear to be measurement artifacts unique to our smooth-bed experiments. Close-up videotapes of these experiments reveal that ~5 mm gaps in the flume bed 0.18 m upslope from the

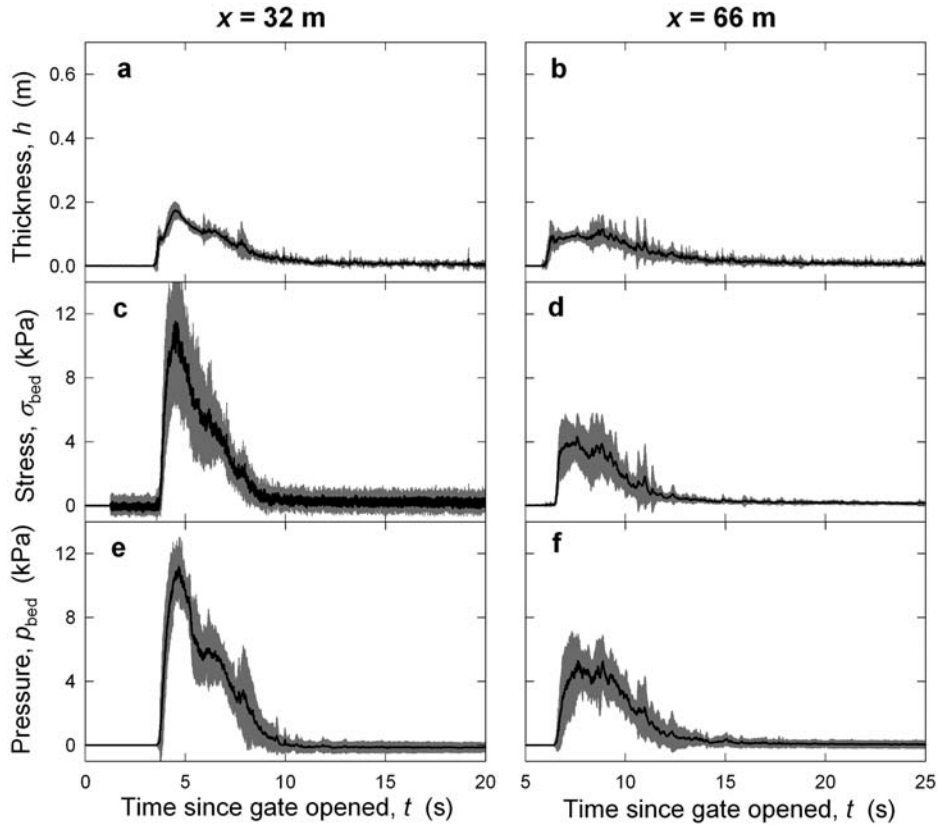

Figure 14. Aggregated time series data for SG smooth-bed experiments. Mean values (black lines) and standard deviations (gray shaded areas) are shown.

center of the sensor plates systematically disturbed the flows, producing subtle but persistent standing waves that locally redirected a small fraction (M) of the downslope flow momentum so that it was normally incident on the plates. The local increase in basal normal stress necessary to reflect this momentum away from the plates can be roughly estimated as $\rho(Mv)^2$ (i.e., about $340M^2$ kPa if $\rho = 2000$ kg/m^3 and $v = 13$ m/s). By this reasoning, an M value no larger than about 0.15 is necessary to explain the measured σ_{bed} and p_{bed} values, a result we consider further in the Discussion section below.

6.5. Roll-Wave Amplitudes

[69] Aggregated time series data summarize the main dynamical features of our experimental debris flows, but they obscure the presence and properties of roll waves that merit attention because of their significant practical implications [*Zanuttigh and Lamberti*, 2007]. Indeed, the standard deviations of h shown in Figures 11, 12, and 14 result partly from data dispersion due to the more-or-less random occurrence of roll waves in every flow. Although a detailed analysis of roll waves is beyond the scope of this paper, we complement our aggregated time series data by summarizing the aggregated numbers and amplitudes of the roll waves.

[70] For each subset of experiments, we use logarithmic scales to plot the cumulative number of roll waves observed at $x = 32$ m and $x = 66$ m as a function of wave amplitude (Figure 15). (Although some waves also existed at $x = 90$ m, we exclude them here because the formation of deposits at $x = 90$ m greatly interfered with wave propagation.) Roughly the same number of roll waves (~100) occurred in each subset of 8–11 flows at each cross section, although more waves generally existed at $x = 66$ m than at $x = 32$ m (Figure 15). Videotape recordings indicated that most waves present at $x = 32$ m persisted at $x = 66$ m, but that some waves coalesced between $x = 32$ and 66 m, and some new waves emerged within this interval. The largest roll wave in each subset of experiments had an amplitude H_w of at least 0.1 m (calculated by the method described in the section on Digital Data Processing), and in one case the largest wave had $H_w > 0.2$ m (Figure 15). Such amplitudes are comparable to the maximum thicknesses of the debris flows (Figures 11–14).

[71] On the logarithmic axes of Figure 15, the cumulative number of waves N_w is a roughly linear function of H_w in most cases. In particular, $N_w = 0.057\ H_w^{-2}$ fits the data for SGM flows on a rough bed at $x = 66$ m remarkably well ($r^2 > 0.99$) (Figure 15b). This inverse power law indicates that the wave amplitudes exhibit a fractal distribution with a fractal dimension of 2 [cf. *Turcotte*, 1992; *Burroughs and Tebbens*, 2001]. We use the same inverse power law as a reference line in the other panels of Figure 15, where it helps illustrate subtle deviations from this fractal distribution.

[72] Relative to the reference line $N_w = 0.057\ H_w^{-2}$, a consistent feature of the data in every panel in Figure 15 is a slightly concave-downward trend, such that the data points for the largest values of H_w plot furthest below the reference line. Such concavity is characteristic of upper-truncated

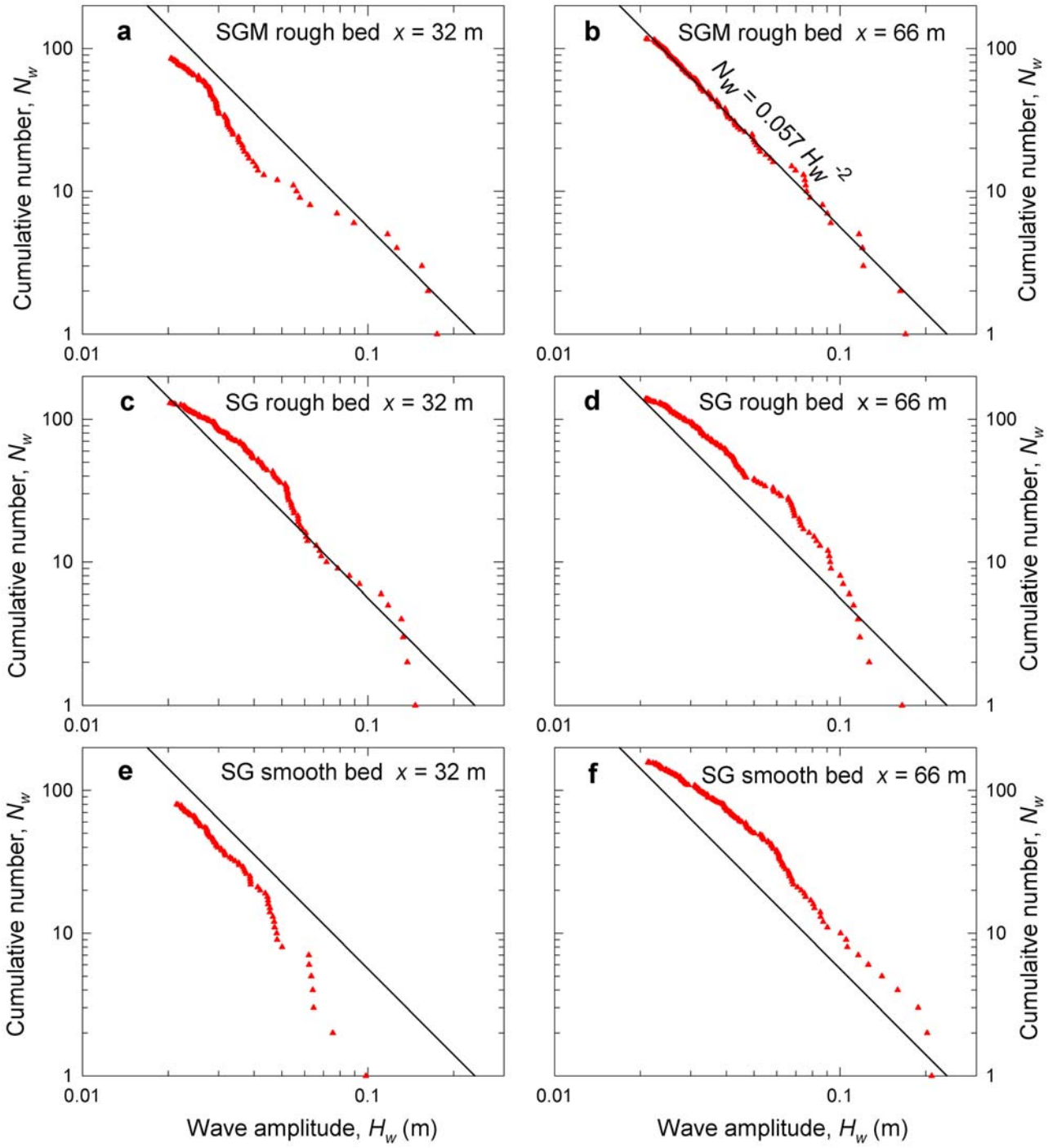

Figure 15. Cumulative number-amplitude distributions of all roll waves with amplitudes >0.02 m measured in each experiment subset. Symbols (red) denote individual waves. Power law regression line (black) computed for data in Figure 15b is shown for reference in every plot.

power laws describing phenomena in which the largest events also constitute the most poorly sampled part of the population [*Burroughs and Tebbens*, 2001]. Viewed in greater detail, the data for x = 32 m consistently exhibit patterns that might be described as dual upper-truncated power laws (Figure 15a, 15c, and 15e): waves with amplitudes smaller than about 0.05 m form tightly clustered, concave trends, and waves with larger amplitudes form looser trends that also exhibit some concavity. We suggest an apparent reason for the single and dual upper-truncated power laws in section 8 below.

6.6. Deposit Morphology

[73] Data depicting the morphology of deposits that formed on the runout pad at the base of the flume cannot be aggregated without significant information loss. Therefore,

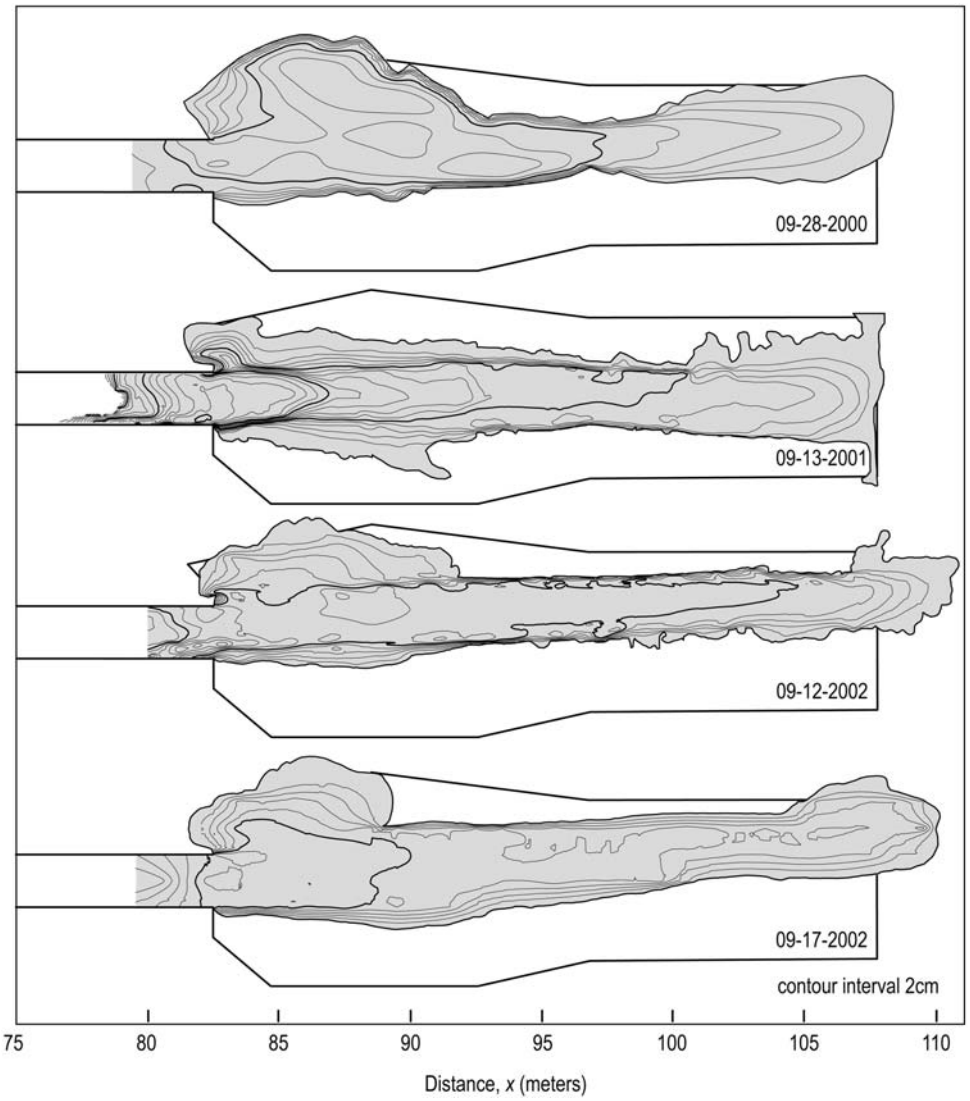

Figure 16. Isopach maps of deposits formed on runout pad in 4 SGM rough-bed experiments. Contour interval is 2 cm. Runout pad topography is shown in Figure 3b.

Figures 16–18 depict isopach maps of individual deposits formed in every experiment in which we did not obstruct or channelize flow on the runout pad. These maps illustrate clear similarities within experiment subsets and clear differences between subsets. Indeed, for any fixed combination of debris composition and bed roughness, the gross morphology of deposits is remarkably reproducible, irrespective of differing details. (We present only two deposit maps for the SG smooth-bed case, because our aggregated data set involves only two SG smooth-bed flows in which we did not tamper with the runout process. *Major* [1996, 1997] and *DeNatale et al.* [1999] presented deposit maps for additional smooth-bed experiments.)

[74] The SGM rough-bed experiments yielded deposits conspicuously longer, thinner, and more tabular than deposits formed in the other experiment subsets. The distal margins of the SGM rough-bed deposits consistently extended to x = 108 to 110 m. The widths of the deposits averaged about 5 m, and thicknesses averaged about 0.1 m (Figure 16). The lateral edges of the deposits were steep in some places (especially near the flume mouth), where well-developed gravel-rich lateral levees formed, and were tapered in other places (especially near the distal margins), where lower levees were overtopped by liquefied, muddy debris that also formed the deposit cores. Drainage of muddy fluid from the deposit core through the deposit margins persisted for many hours as interior pore pressures gradually declined [*Major and Iverson*, 1999].

[75] Deposits formed by the SG rough-bed flows were roughly half as long and twice as thick as those formed by the SGM rough-bed flows (Figure 17). Steep lateral margins formed by gravel-rich levees were most conspicuous in the SG deposits, because the levees were rarely overtopped by trailing, liquefied debris. Although pore pressure data collected beneath the SG rough-bed deposits at x = 90 m indicate that the debris there was not fully saturated (Figure 13f), the sensors at x = 90 m were located close to the gravel-rich, distal deposit margins, where lack of high pore pressure was unsurprising [cf. *Major and Iverson*, 1999]. The large standard deviations of basal sensor data collected at x = 90 m also

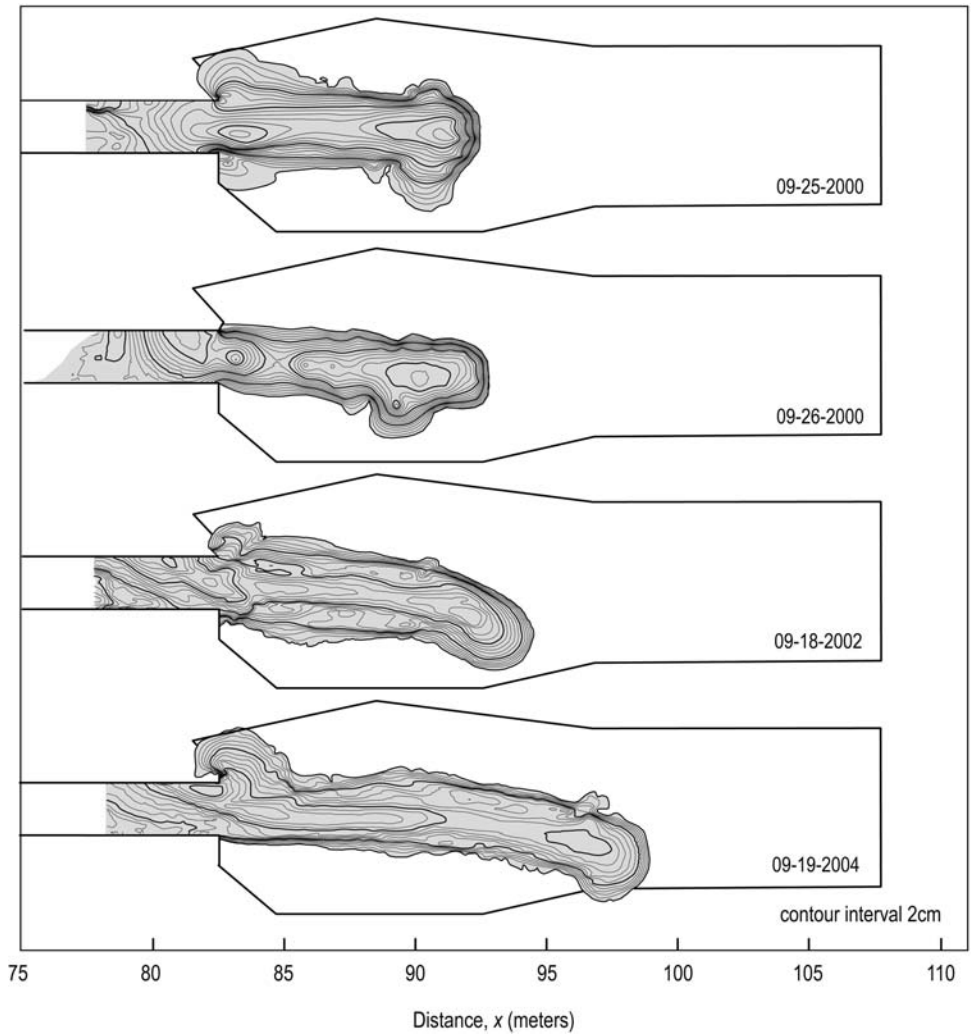

Figure 17. Isopach maps of deposits formed on runout pad in 4 SG rough-bed experiments. Contour interval is 2 cm.

reflect the sensitivity of measurements to margin proximity (Figure 12).

[76] Relative to the other experiment subsets, the SG-smooth-bed flows produced broad deposits less constrained by lateral levees (Figure 18). The lack of pronounced levees enabled the SG-smooth-bed flows to lose downslope momentum quickly as they moved onto the runout pad and spread laterally. As a consequence, the runout distances of SG-smooth-bed flows were very similar to those of SG-rough-bed flows, despite the fact that the smooth-bed flows had front speeds about 30 percent larger than those of the rough-bed flows when they reached the break in slope at x = 74 m (Figure 9).

7. Implications for Modeling

[77] We use the mathematical model summarized in section 2 to examine further implications of our data. We emphasize data from our SGM rough-bed debris flows, because their relatively high mud contents and rough basal boundaries most closely resembled those of debris flows in nature.

7.1. Evolution of Flow Bulk Density

[78] The aggregated mean time series data from our SGM rough-bed experiments (Figures 13a–13c) provide a basis for estimating evolving flow bulk densities as well as all right-hand-side (RHS) terms in (2). Estimation of these quantities requires calculation of products, differences or derivatives of time-dependent data, and to reduce noise in these calculations, we first smooth the 100-Hz data by applying a 100-point moving median [*Press et al.*, 1986, p. 497]. This smoothing yields the time series $h(t)$, $\sigma_{bed}(t)$ and $p_{bed}(t)$ shown as bold curves in Figures 19a–19c.

[79] We next use the smoothed time series to calculate time-dependent bulk densities $\rho(t)$ by assuming that $\sigma_{bed}(t)$ approximately balances the slope-normal component of the static weight of the debris, such that:

$$\rho(t) \approx \frac{\sigma_{bed}(t)}{gh(t)\cos\theta}. \tag{10}$$

Results from this formula show that $\rho(t)$ increases almost monotonically from 0 to about 2000 kg/m^3 during passage

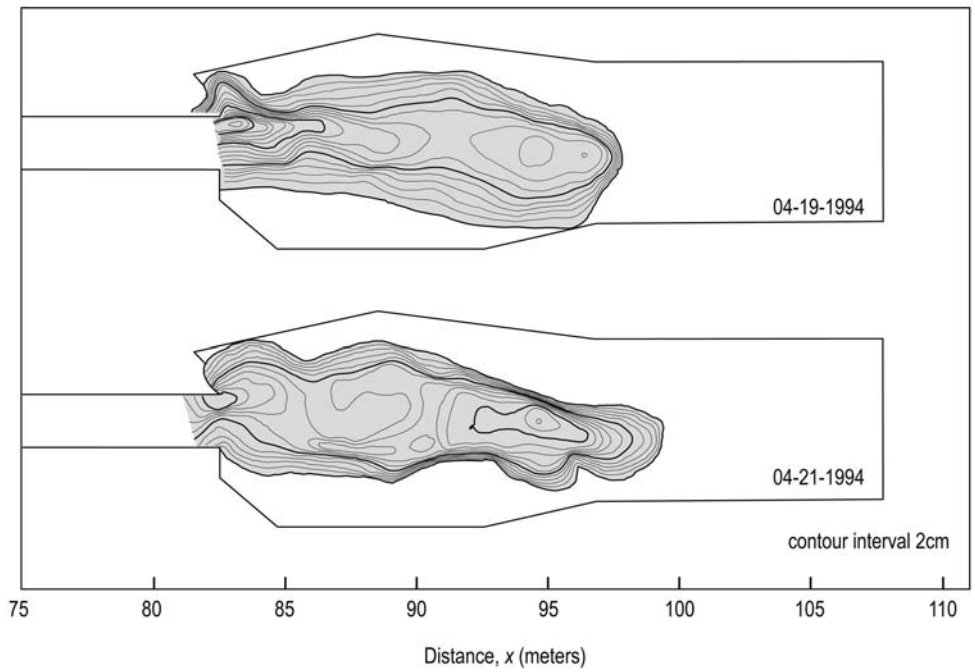

Figure 18. Isopach maps of deposits formed on runout pad in 2 SG smooth-bed experiments. Contour interval is 2 cm.

of dilated flow fronts at x = 32 and 66 m (Figures 19d and 19e). Strong variation of $\rho(t)$ becomes focused in a narrowing domain as debris flows travel downslope, and at x = 90 m, $\rho(t)$ remains nearly constant after passage of a contracted flow front (Figure 19f). In general, however, Figures 19d–19f show that $\partial\rho/\partial t \sim 1000$ kg/m^3-s is common during front passage, and this bulk density evolution produces strong forcing effects on the RHS of equations (1) and (3) in addition to important effects in the momentum balance (2).

[80] If significant acceleration normal to the bed were present, as may be true for natural debris flows in irregular channels, then (10) would be a poor approximation because the effective weight of the debris would be modified [cf. *Denlinger and Iverson*, 2004]. We have no reason to suspect this effect in our experimental data, however, except as the previously noted measurement artifact in our SG smooth-bed time series.

7.2. Evolution of Flow Resistance

[81] Evaluation of right-hand-side (RHS) terms in momentum-balance equations such as (2) is one of the most fundamental yet elusive tasks necessary to quantify debris-flow mechanics. We estimate evolving values of the RHS terms in (2) by combining the values of $\rho(t)$ shown in Figures 19d–19f with those of the smoothed time series data $h(t)$, $\sigma_{bed}(t)$, and $p_{bed}(t)$ shown in Figures 19a–19c, and by applying the formulas:

Driving force per unit basal area,

$$\rho gh \sin\theta \approx \rho(t)gh(t)\sin\theta; \tag{11}$$

Granular (Coulomb) basal shear stress,

$$-\tau_s \approx -[\sigma_{bed}(t) - p_{bed}(t)]\tan\phi_{bed}; \tag{12}$$

Fluid basal shear stress,

$$-\tau_f \approx -\mu[\overline{v}/h(t)] + \tau_y; \tag{13}$$

Granular longitudinal stress,

$$-\kappa\rho gh\cos\theta\frac{\partial h}{\partial x} \approx -\kappa\rho(t)gh(t)\frac{h_{t+1} - h_{t-1}}{2\overline{v}\Delta t}; \tag{14}$$

Fluid longitudinal stress,

$$-(1-\kappa)h\frac{\partial p_{bed}}{\partial x} \approx -(1-\kappa)h(t)\frac{p_{bed\ t+1} - p_{bed\ t-1}}{2\overline{v}\Delta t}. \tag{15}$$

[82] To evaluate these formulas we use our geotechnical test results to specify that $\phi_{bed} = 40°$, $\kappa = 2.4$ (as implied by (8) and the condition $\phi_{\rm int} = \phi_{bed}$), μ = 0.1Pa-s, and $\tau_y = 0$, implying that the viscosity of the pore fluid is 100 times greater than that of pure water, but that the debris lacks any intrinsic yield strength. We approximate the flow velocity with the fixed values $\overline{v}$ = 10 m/s at x = 32 and 66 m and $\overline{v}$ = 3 m/s at x = 90 m, and as shown in (14) and (15), we use finite difference formulas to approximate partial derivatives. Furthermore, in these central difference formulas we approximate spatial steps (Δx) with advected time steps ($\overline{v}\Delta t$) because we lack direct knowledge of Δx.

[83] The most significant results of our RHS calculations are shown by heavy black lines depicting evolution of the summed basal stress terms, $\Sigma_{base} = \rho gh \sin\theta - \tau_s - \tau_f$ (Figures 19g–19i). At x = 32m, $\Sigma_{base} > 0$ applies throughout the flow duration, and the small difference between Σ_{base} and $\rho gh \sin\theta$ implies that the flow can behave almost like a frictionless mass (Figure 19g). At x = 66 m, in contrast,

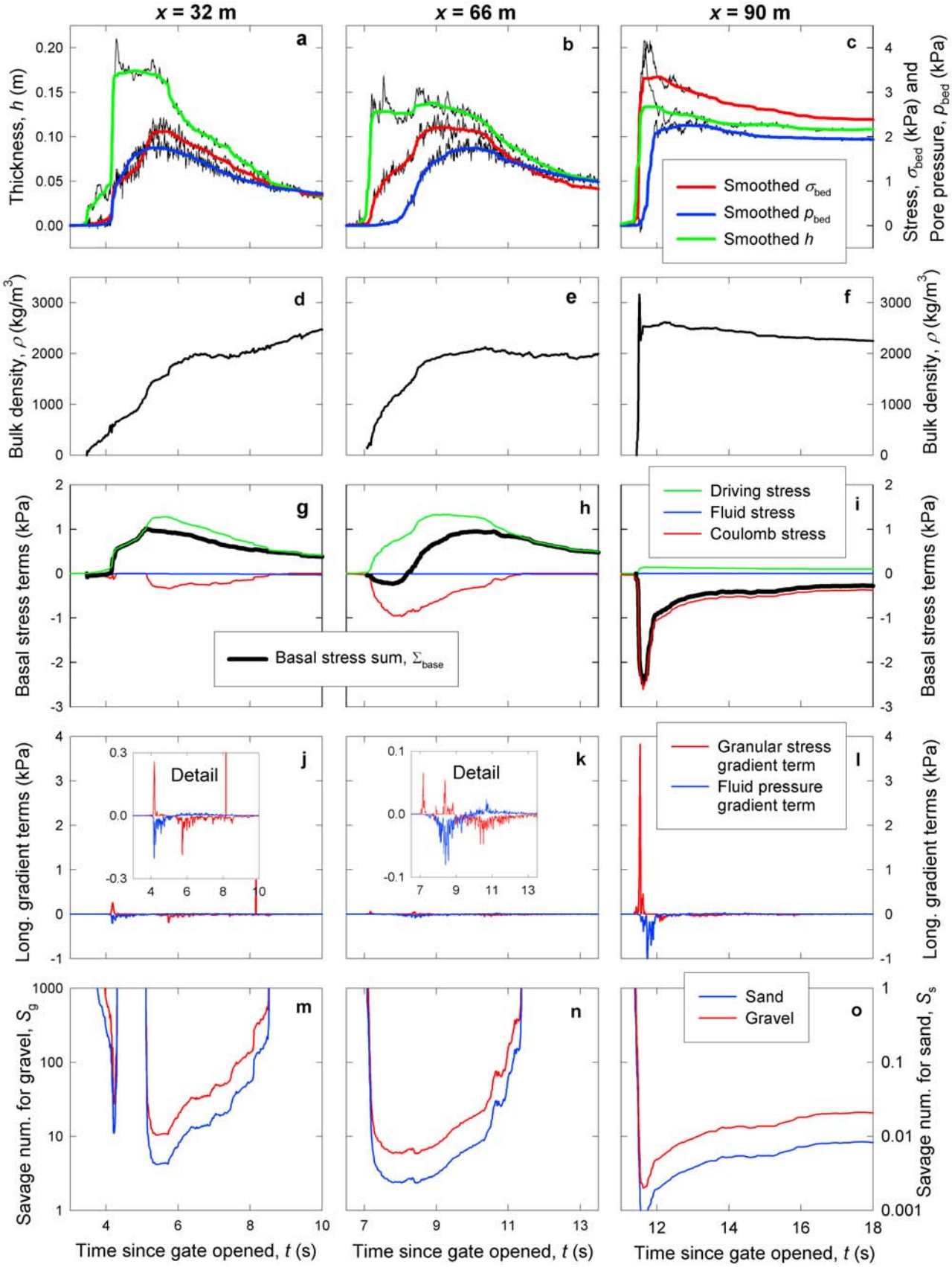

Figure 19. (a–c) Smoothed, aggregated time series data for SGM rough-bed experiments; (d–o) mechanical quantities calculated from the smoothed data.

$\Sigma_{base} < 0$ applies for roughly 1 s as the flow front passes, and this deficit in Σ_{base} demonstrates the degree to which the flow front's basal friction impedes downslope motion of the trailing part of the flow (Figure 19h). At $x = 90$ m, $\Sigma_{base} < 0$ is pervasive, with particularly large net resistance focused at the flow front.

[84] Additional driving and resisting effects can result from the influence of RHS terms that express longitudinal stress gradients (Figures 19j–19l), which can locally be very significant. Indeed, for the leading edge of the debris mass initially loaded behind the headgate, the values $\partial h/\partial x \approx -3.3$ and $\kappa \approx 1$ apply, indicating the existence of a downslope driving force at least 5 times greater than that due to gravity alone. After the debris flows have traveled to $x = 32$ and 66 m, however, the longitudinal gradient terms are generally $\ll \Sigma_{base}$ (Figures 19j and 19k). At $x = 90$ m the contributions of longitudinal stress gradients again become significant, because a steepened gradient of h in the coarse granular snout helps drive motion forward, while an opposing gradient in p_{bed} just behind the snout hinders forward motion (Figure 19l). The effects of these gradients on the momentum balance are comparable to those of Σ_{base} for ~1 s as the flow front passes (Figures 19i and 19l).

[85] Along with the evolving RHS terms, we calculate evolving values of the Savage number, S (Figures 19m–19o). In this calculation we use the approximation $\dot{\gamma} \approx \overline{v}/h(t)$ in (5), yielding:

$$S \approx \frac{\rho_s \overline{v}^2}{\sigma_{bed}(t) - p_{bed}(t)} \left(\frac{\delta}{h(t)}\right)^2. \tag{16}$$

We apply this formula using two characteristic values of δ for our sediment mixtures: the modal size of gravel ($\delta = 20$ mm) yields S_g, and the modal size of sand ($\delta = 0.4$ mm) yields S_s. We find that generally $S_g > 10$ and $S_s < 0.1$, implying that inertial grain collisions dominate grain-contact stresses in the gravel fraction, but not in sand. Flow fronts composed mostly of gravel consequently might exhibit Coulomb frictional resistance as much as 50 percent larger than that implied by our measured values of ϕ_{int} and ϕ_{bed} [*Forterre and Pouliquen*, 2008]. A further complication is that both S_g and S_s become infinite when complete liquefaction occurs (i.e., $\sigma_{bed}(t) - p_{bed}(t) \rightarrow 0$). As a result, enduring grain-contact stresses vanish entirely, but they may be replaced by grain-collision stresses that mimic the shear-to-normal stress proportionality of Coulomb stresses [*Bagnold*, 1954; *Takahashi*, 1981; *Hunt et al.*, 2002]. We lack direct measurements of collisional stresses, however, and as a consequence, the magnitudes of τ_s shown in Figures 19g–19i represent minimum values based on Coulomb friction and our measured values of $\sigma_{bed}(t) - p_{bed}(t)$ and ϕ_{bed}.

7.3. Evolution of Flow-Front Speeds

[86] The speed of flow-front propagation is one of the most readily observable and practically important aspects of debris-flow motion. Owing to the dominant effects of the basal stress terms (Σ_{base}) evident in Figure 19, a relevant hypothesis is that flow-front propagation might be modeled adequately by a simple momentum balance that neglects evolution of all quantities except v. In this case (2) reduces to a zero-order (in ε) approximation describing motion of a rigid mass resisted only by basal stresses:

$$\rho h \frac{dv}{dt} = \Sigma_{base} = \rho g h[\sin\theta - (1-\lambda)\cos\theta\tan\phi_{bed}] - \left(\tau_y + \mu\frac{v}{h}\right). \tag{17}$$

[87] On the RHS of (17) we introduce the degree of liquefaction,

$$\lambda = p_{bed}/\rho g h \cos\theta, \tag{18}$$

to represent the normalized influence of basal pore pressure on Coulomb resistance, and we embed (6) to include terms representing the effects of fluid shearing on basal flow resistance.

[88] To compare predictions of (17) with the mean flow-front propagation data for our experimental debris flows (Figure 9), we substitute $v = dx/dt$ in (17) and integrate the equation twice to obtain the downslope coordinate (x) of an advancing mass as a function of time:

$$x = \frac{\sin\theta - (1-\lambda)\cos\theta\tan\phi_{bed} - \tau_y/\rho g h}{B} \cdot \left[t - \frac{1}{Bg}(1 - \exp(-Bgt))\right]. \tag{19}$$

Here $B = \mu/\rho g h^2$, but in the special case with $B = 0$ (i.e., inviscid pore fluid), (19) is replaced by

$$x = \frac{1}{2} g t^2 [\sin\theta - (1-\lambda)\cos\theta\tan\phi_{bed} - \tau_y/\rho g h]. \tag{20}$$

We construct graphs of (19) and (20) by using parameter values grossly representative of flow fronts in our experiments: $h = 0.2$ m, $\rho = 2000$ kg/m^3, $\theta = 31°$, and $\phi_{bed} = 40°$; and by using either representative or extreme values of λ, τ_y, and μ (Figure 20). The graphs show that predictions of the rigid-body model fit the data most closely if λ lies within the realistic range 0.8–1, whereas the fit is affected little by τ_y ranging from 0 to 100 Pa, and by μ ranging from 0 to 10 Pa-s. Thus, the results shown in Figure 20 imply that solid-phase friction dominates basal resistance in the momentum balance.

[89] More striking than the fit of any curve in Figure 20, however, is the systematic deviation of all curves from the trends of the data. For $t < \sim 3$ s, the data generally lie closest to the curve computed for frictionless motion, but the data for the SG smooth-bed experiments plot slightly above this curve. In other words, near $t = 0$, flow fronts on smooth beds move downslope faster than an ideal, frictionless body. This remarkable behavior results from the large initial influence of the downslope driving effect caused by longitudinal stress gradients that are neglected in the rigid-body model. This driving effect quickly diminishes, however, and for $t > \sim 3$ s, the data in Figure 20 consistently follow trends below those of all the theoretical curves, regardless of the values of basal resistance parameters. We infer that evolution and heterogeneity of flow resistance cause flow-front motion to differ

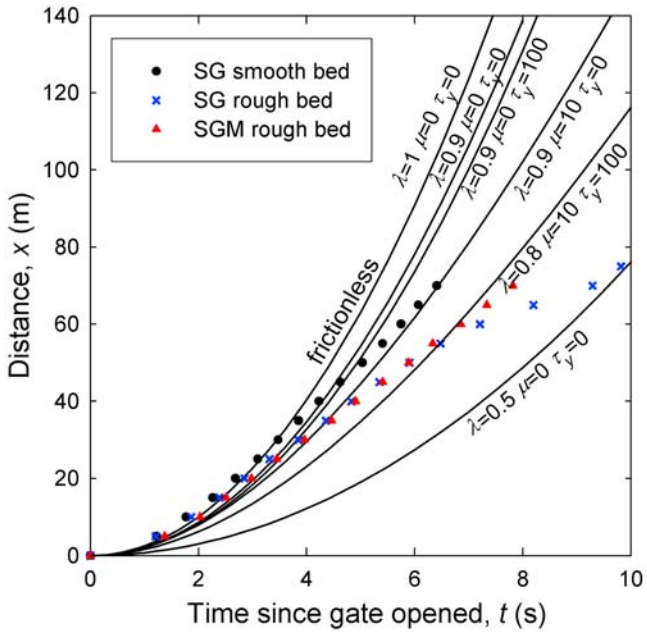

Figure 20. Comparison of flow-front motion calculated using a rigid-body model (curves) with mean values measured in three experiment subsets (data points). Units of the model parameters τ_y and μ are Pa, and Pa-s, respectively. Data points are the same as those shown in Figure 9.

qualitatively as well as quantitatively from that predicted by (17).

7.4. Evolution of Longitudinal Stress Gradients

[90] Longitudinal stress gradients can at times be large enough to contribute significantly to driving and resisting effects, and the right-hand side of (2) implies that these gradients have two components, one that depends on grain-contact stresses (involving $-\kappa\ \partial h/\partial x$) and one that depends on pore fluid pressure (involving $(1-\kappa)\ \partial p_{bed}/\partial x$). Longitudinal gradients in intergranular compressive stresses produce a downslope driving force where $\partial h/\partial x < 0$, and produce resistance where $\partial h/\partial x > 0$. The driving effect is greatest at the time of flow release, when the magnitude of $\partial h/\partial x$ is largest and flow-front acceleration is very rapid, as discussed above.

[91] Declining flow-front acceleration at later times ($t >$ ~3 s in Figures 19 and 20) results partly from the diminishing magnitude of $\partial h/\partial x$, but also from the increasing influence of nonuniform pore pressure distributions. To highlight this influence, we recast the longitudinal stress gradient terms in (2) in a form that employs the degree of liquefaction, λ, defined in (18):

$$-\kappa\rho gh\cos\theta\frac{\partial h}{\partial x}-(1-\kappa)h\frac{\partial p_{bed}}{\partial x} = \rho gh\cos\theta\left(-\kappa\frac{\partial h}{\partial x}-(1-\kappa)\left[\lambda\frac{\partial h}{\partial x}+h\frac{\partial\lambda}{\partial x}\right]\right). \quad (21)$$

The right-hand side of (21) shows that if λ is uniform, the effect of pore pressure on the longitudinal stress gradient is relatively simple: the gradient ranges from $-\kappa\ \rho gh\cos\theta(\partial h/\partial x)$ in the case with $\lambda = 0$ to $-\rho gh\cos\theta(\partial h/\partial x)$ in the fully liquefied case with $\lambda = 1$. If the degree of liquefaction is nonuniform, however, additional effects are encapsulated by the last term in (21). For $\partial\lambda/\partial x < 0$ and $\kappa > 1$ (the values applicable in the heads of our debris flows on rough beds), $\partial\lambda/\partial x$ produces resistance to downslope motion, even where $\partial h/\partial x < 0$. This local resistance contributes to development of debris-flow snouts that are steeper and deeper than those of either watery flash floods or dry granular avalanches of comparable volume.

7.5. Evolution of Basal Pore Fluid Pressure

[92] The foregoing results demonstrate the great importance of pore fluid pressure on debris-flow mechanics, and high pore pressures in our experiments are generated by the initial contractive failure of loosely packed debris [*Iverson et al.*, 2000]. Mud in the debris promotes pore pressure persistence by lowering the hydraulic diffusivity, D, thereby reducing the magnitude of dp_{bed}/dt in the pore pressure evolution equation, (3) [*Iverson*, 1997; *Major et al.*, 1997; *Major*, 2000]. The effect of D can be illustrated mathematically by assuming that ρ and h are constant (as in (17)), in which case (3) simplifies to:

$$\frac{dp_{bed}}{dt} = -\frac{2D}{h^2}p_{bed}+\frac{2D}{h}\rho_f g\cos\theta. \quad (22)$$

This equation has a solution indicating that, in a Lagrangian reference frame moving with velocity v, p_{bed} relaxes from an arbitrary initial value p_0 toward the hydrostatic equilibrium value $\rho_f gh\cos\theta$ according to:

$$\frac{p_{bed}-\rho_f gh\cos\theta}{p_0-\rho_f gh\cos\theta} = \exp\left(\frac{-2Dt}{h^2}\right). \quad (23)$$

The exponential dependence of pore pressure relaxation on D underscores its importance in regulating Coulomb friction.

[93] The implications of D for pore pressures measured in our experiments can be evaluated by determining the relaxation timescale $h^2/2D$ in (23) for our two sediment mixtures. For the SGM mixture, the value of D measured in quasistatic slurry consolidation tests is about 1.3×10^{-6} m^2/s [*Major et al.*, 1997; *Major*, 2000]. Used in conjunction with a typical flow thickness $h = 0.1$ m, this D value yields $h^2/2D \approx$ 4000 s, a relaxation time that explains the maintenance of high pore pressures once they are established in the muddy bodies of our SGM flows (Figures 11 and 13). Our attempts to similarly measure D in the SG mixture were thwarted by the difficulty of maintaining a quasistatically slurried state, but for this mixture a calculated value of D is about 4×10^{-4} m^2/s [*Iverson*, 1997]. Used in conjunction with $h = 0.1$ m, this value yields $h^2/2D \approx 12$ s, a relaxation time consistent with our measurements of quickly diminishing pore pressures in our SG debris flows (Figures 12 and 13).

8. Discussion

[94] Our experimental debris flows differed from natural debris flows in several respects, but they consistently developed the characteristic head-and-body architecture long recognized in natural debris flows in diverse settings [*Stiny*, 1910; *Sharp and Nobles*, 1953; *Pierson*, 1986; *Takahashi*, 1991]. The dam-break onset of our experimental

flows caused them to accelerate almost like frictionless masses for ~3 s, but in the subsequent ~4 s the flows' motion largely equilibrated with their frictional resistance, as evidenced by nearly constant front velocities, peak depths, and flow durations. Perhaps the most important difference between our experimental flows and many natural debris flows derived from the absence of erodible boundaries and sediment entrainment. This absence promoted reproducibility of results, however, yielding clear targets for model predictions.

[95] Development of variable pore fluid pressures resulted in nonuniform degrees of liquefaction in our experimental debris flows, with large implications for the distribution of basal friction and evolution of flow momentum. The bodies of the debris flows were largely liquefied by high pore pressure, whereas mature flow fronts lacked positive pore pressure entirely. Measurements of similar pore pressure distributions in natural debris flows reinforce the relevance of this observation [*McArdell et al.*, 2007]. In fact, we believe the prominent role of evolving, heterogeneous pore fluid pressure is the chief mechanical trait distinguishing debris-flow behavior from that of granular avalanches that lack significant pore fluid pressure [cf. *Iverson et al.*, 2004]. An intermediate style of behavior might be represented by our mud-poor SG flows, in which high pore pressures developed but dissipated quickly.

[96] Owing to enhanced maintenance of high pore pressures, our SGM debris flows had bulk mobilities exceeding those of our SG flows, regardless of whether mobility was gauged by flow speed, runout distance, or the area inundated. The high mobility of the muddy flows is consistent with the results of rheometric experiments in which the addition of small (colloidal) particles enhances lubrication forces that reduce friction between larger grains [*Ancey*, 2001]. In contrast, other small-scale experiments show that systematic increases in mud content can cause systematic increases in flow resistance due to increased debris yield strength and viscosity [e.g., *Johnson*, 1970; *O'Brien and Julien*, 1988; *Coussot and Proust,* 1996; *Parsons et al.*, 2001]. Our findings imply that such effects can dominate at miniature scales, whereas the effects of mud on pore fluid pressure and friction reduction are more likely to dominate when the scale is more realistic.

[97] Our data highlight the evolution not only of pore pressure but also of flow bulk density ρ and porosity n. Inferred values of ρ varied monotonically from 0 to about 2000 kg/m^3 during passage of dilated, coarse-grained flow fronts, and for liquid-saturated debris, a bulk density increase $\Delta\rho = 1000$ kg/m^3 implies a porosity decrease $\Delta n = -\Delta\rho/(\rho_s - \rho_f) \approx -0.6$. For unsaturated debris the analogous porosity decrease is no smaller than $\Delta n = -\Delta\rho/\rho_s \approx -0.4$. Such large changes in ρ and n reflect concomitant changes in flow agitation and grain-size segregation, and they have profound ramifications for gravitational stresses, grain-collision stresses, and evolution of pore pressure. Indeed, we infer that ρ (or n) is a fundamental state variable in debris flows, and that predicting evolution of ρ and n is critical for predicting evolution of v, h, and p_{bed} [cf. *Kowalski*, 2008; *Pailha and Pouliquen*, 2009; *Iverson*, 2009].

[98] Grain-size segregation and evolution of ρ and p_{bed} during debris-flow motion raise questions about the attendant distribution of hydraulic diffusivity, D. An assumption implicit in equation (3) governing dp_{bed}/dt is that D and p vary only gradually in the x direction, such that $D(\partial^2 p/\partial y^2) \gg D(\partial^2 p/\partial x^2) + (\partial D/\partial x)(\partial p/\partial x)$ is satisfied [*Savage and Iverson*, 2003]. We lack direct measurements of the terms in this inequality, but the large values of $\partial\rho/\partial t$ and $\partial p_{bed}/\partial t$ evident from our data lead us to suspect that it is violated. Our debris-flow models currently assume that D is a prescribed function of x [e.g., *Iverson and Denlinger*, 2001; *Denlinger and Iverson*, 2001; *Savage and Iverson*, 2003], but development of more complete models that predict the distribution of D in response to evolving grain-size segregation is clearly warranted.

[99] Although grain-size segregation in our experimental debris-flow deposits is well-documented [*Major*, 1996, 1997; *Major and Iverson*, 1999], most models lack any means of predicting the segregation process itself. Recent development of evolution equations describing transport of grains of differing sizes in granular avalanches shows considerable promise [*Thornton and Gray*, 2008; *Gray and Ancey*, 2009], but our current inability to measure or compute the dynamics of size segregation in debris flows reflects a lack of basic data and understanding.

[100] In our experiments with rough beds, the nearly liquefied debris behind flow fronts exerted basal normal stresses roughly proportional to the debris weight ($\sigma_{bed} \approx \rho g h \cos\theta$), but basal shear stresses exerted by this debris are more equivocal. *Bagnold* [1954] found that intergranular shear stress remains proportional to intergranular normal stress in liquefied (i.e., "gravity-free") grain-fluid mixtures, an inference that has withstood repeated scrutiny [*Hunt et al.*, 2002]. Bagnold's findings provide only partial guidance for predicting the granular contribution to shear stress in debris flows, however, because they offer no basis for predicting the granular contribution to the total basal normal stress in a liquefied, free-surface flow driven by gravity. Although recent theoretical analyses provide clues to this behavior [e.g., *Berzi and Jenkins*, 2008], a clear need exists for more direct measurements of basal shear stress along with basal normal stress [e.g., *McArdell et al.*, 2007].

[101] Basal stress and pore pressure data from our smooth-bed experiments suffered from a measurement artifact, but the cause and magnitude of the artifact have important physical implications. The smooth-bed data show that even small momentum components systematically directed normal to the bed can cause basal stresses to differ by a factor >2 from those expected from geostatic loading. In view of this sensitive behavior, it's perhaps surprising that basal normal stresses measured in our rough-bed experiments largely conformed with expectations based on the geostatic approximation, $\sigma_{bed} \approx \rho g h \cos\theta$. We believe this conformity is explained by flow agitation that occurs in the presence of a bumpy basal boundary. Bumps cause irregular motions of grains that contact the bed, thereby decreasing the likelihood of coherent standing waves or other sources of organized bed-normal acceleration. As in a classical gas, the disorganized motion of a large number of interacting particles can regularize boundary stress measured macroscopically [*Goldhirsch*, 2003].

[102] The localized departures from $\sigma_{bed} \approx \rho g h \cos\theta$ measured in our smooth-bed experiments may also have implications for boundary erosion in situations where an erodible bed is present. Substantial stress concentrations that

occur in the presence of even subtle standing waves could promote localized entrainment or deposition in natural, sediment-lined debris-flow channels.

[103] Roll waves were a ubiquitous, readily measured phenomenon in each of our experimental debris flows, but our interpretation of the waves relies on qualitative observations. Although most of the waves appeared to grow from infinitesimal perturbations, as expected from classical stability analyses [*Zanuttigh and Lamberti*, 2007], the single largest wave in each flow generally had a non-classical origin. This wave developed because the last debris to evacuate the headgate area was typically the most watery. The watery debris overtook high-friction, coarse-grained debris in its path, pushed it forward to form a wave, coalesced with smaller waves, and eventually produced a wavefront with a height comparable to the maximum flow thickness. Our aggregated time series data preserve muted evidence of these large waves (near t = 5.5 s in Figure 13a and t = 8.5 s in Figure 13b, for example), but their presence is more apparent in cumulative number-size distributions (Figure 15). In these distributions about 8 to 10 large waves (one per flow) form subpopulations somewhat distinct from those of smaller waves. The distinction is most prominent at x = 32 m, where the subpopulations of large and small waves define dual concave-downward curvatures indicative of upper-truncated power laws [cf. *Burroughs and Tebbens*, 2001] (Figures 15a, 15c, and 15e).

[104] At x = 66 m the subpopulations of large and small roll waves nearly merge into a single, less-concave population (Figures 15b, 15d, and 15f). The merger appears to reflect a maturation of fractal wave-height distributions, implying that roll waves of all sizes (up to the flow thickness) occur in cumulative numbers that decline in proportion to the square of the wave amplitude. A practical ramification is that these waves represent a type of scale-free randomness, which could be superposed on deterministic predictions that otherwise neglect the presence of roll waves.

[105] Patterns of debris-flow runout and deposition at the base of the flume reflected patterns of behavior upslope, and the imprint of bed roughness was particularly distinctive. Roughness promoted granular agitation and grain-size segregation, and segregation in turn promoted formation of gravel-rich lateral levees. Gravelly roll-wave fronts also contributed to levee growth, and in some cases formed multiple generations of nested levees. Levees helped preserve downslope momentum by inhibiting lateral spreading during runout, as is evident in morphologies of deposits (Figures 16–18). The fact that SG flows on rough beds ran out as far as SG flows on smooth beds (despite considerably smaller flow speeds on rough beds) testifies to the levees' importance.

[106] A more subtle but nevertheless consistent imprint on the planimetric forms of deposits arose from small imperfections in flume geometry. Deposits in all SGM rough-bed experiments had prominent side lobes extending markedly to the left (i.e., toward the top in Figure 16) near the flume mouth, and distal deposition was skewed progressively leftward. Videotape records show that both asymmetries were attributable to the effects of the 2° leftward tilt of the flume bed. The bed tilt caused the gravel-rich leading edges of nearly all flows to migrate to the left as they traveled beyond about x = 40 m (i.e., to the right in the upslope view of Figure 1). The leading edges of flows decelerated when they passed the break in slope at x = 74, and then, beginning around x = 80 m, they deposited gravel-rich wedges of static debris on the flume bed, mostly against the left flume wall. These small wedges ($\ll$1 m^3) deflected trailing debris slightly to the right, and as this debris issued from the mouth of the flume at x = 82.5 m, it formed well-developed, gravel-rich lateral levees preferentially on the right. It formed somewhat lower lateral levees on the left, and overtopping of the left-side levees by trailing surges of more-dilute debris produced the left-side lobes deposited just beyond the flume mouth. The larger right-side levees directed most of the distal deposition subtly to the left, and a slight leftward tilt of the runout pad beyond x = 95 m probably added to this skewing (Figure 3b).

[107] In contrast, deposits of SG rough-bed flows were skewed distally to the right, although they, too, had proximal left-side lobes due to levee overtopping (Figure 17). A subtle rightward tilt of the runout pad where the SG flows slowed significantly (between about x = 90 and 95 m; Figure 3b) may have been responsible, but this same tilt had no noticeable effect on the SGM rough-bed flows, which maintained their downslope momentum well past x = 95 m. We infer that depositional patterns were remarkably sensitive to nuances in flume geometry.

9. Conclusions

[108] The mean values of our aggregated time series data illustrate the central tendencies of debris-flow behavior when initial and boundary conditions are macroscopically controlled, and the data dispersion reveals the effects of uncontrollable details. For each of our experiment subsets, the means of the aggregated data are generally much larger than the standard deviations, implying that the main features of our experimental debris flows are reproducible. As a result, our aggregated data provide clear targets for tests of predictive models.

[109] Our data demonstrate that a key feature of debris-flow behavior is development and persistence of dilated, high-friction, coarse-grained flow fronts, pushed from behind by nearly liquefied, finer-grained debris. In our experiments this heterogeneous flow architecture appears during the first ~30 m of motion, matures within the next ~30 m, and greatly influences subsequent flow deceleration and deposition. As heterogeneity develops, local flow resistance and global flow dynamics evolve simultaneously. Feedbacks coupling local resistance and global dynamics imply that conventional rheological models have limited relevance for interpreting and predicting debris-flow behavior.

[110] Imposed differences in bed roughness and sediment mud content in our experiments cause systematic differences in flow dynamics, some expectable and some surprising. Debris flows on smooth beds travel about 30 percent faster but no further than flows on rough beds, and mud-rich flows run out nearly twice as far as mud-poor flows, even though both reach similar peak speeds. Mud reduces net flow resistance by promoting persistence of high pore pressures in flow bodies. Bed roughness increases flow runout by promoting development of coarse-grained flow fronts and

gravel-rich lateral levees, which channelize flow and reduce loss of downslope momentum.

[111] Grain-size segregation in debris flows is more than a source of distinctive morphological and sedimentological features, however; it fundamentally affects flow dynamics. The large size of grains in flow fronts favors inertial grain collisions that increase frictional resistance, and the presence of large intergranular pores implies the existence of high hydraulic diffusivities. High diffusivities facilitate dissipation of excess pore fluid pressure and drainage of pores, adding further to local flow resistance. Additional work is needed to evaluate the cause of segregation and its effects on evolution of hydraulic diffusivity.

[112] Our data also provide documentation of evolving debris porosities and bulk densities. Measured ratios of basal normal stress to flow thickness imply that the leading edges of the experimental debris-flow fronts are highly dilated, reinforcing the inference that collisional momentum exchange is significant. Following passage of dilated fronts, bulk densities stabilize near ~2000 kg/m^3, consistent with expectations for typical debris-flow slurries [*Major and Pierson*, 1992]. Variation of bulk density affects the balances of mass and momentum as well as pore pressure evolution, and prediction of these effects is desirable in the next generation of debris-flow models.

[113] In accord with shallow-flow scaling, longitudinal normal-stress gradients generally play a subordinate role in our experimental debris flows, but their effects nevertheless can at times be crucial. Effects of longitudinal gradients are especially pronounced during flow initiation, when the steepness of flow fronts can drive them downslope at speeds surpassing those of frictionless bodies. Front speeds stabilize at nearly steady values as flow thicknesses diminish, but longitudinal gradients again become significant during flow deceleration. Then, gradients in pore pressure just behind gravelly flow fronts provide resistance that counteracts the driving effect of steepening flow-front faces. A practical ramification for debris-flow hazards is that longitudinal stress gradients help steepen and deepen surge fronts of debris flows relative to those of homogenous water floods or dry granular avalanches.

[114] Surface waves similar to classical roll waves occur in all of our experimental debris flows. They develop gravelly fronts resembling the main flow front, and also develop finer-grained trailing bodies. Waves with diverse amplitudes occur, as demonstrated by their fractal number-size distributions. The largest waves have amplitudes similar to the total flow depth, and they affect flow runout and deposition. Despite the randomizing influences of roll waves, however, the extent and general morphology of our experimental debris-flow deposits are remarkably reproducible.

[115] In summary, our data lead us to conclude that many textbooks misrepresent debris-flow mechanics almost entirely. They commonly attribute the distinctive behavior of debris flows to a fixed, non-Newtonian rheology [e.g., *Allen*, 1997; *Ritter et al.,* 2002], and they generally assume that flows are laminar and subject to no-slip boundary conditions, such that effects of bed roughness are negligible. In contrast, our data demonstrate that the central feature of debris-flow mechanics is heterogeneous two-phase flow, in which boundary friction is crucial and local flow resistance is a variable that evolves together with global flow dynamics. Reproducibility of this emergent behavior implies that, although debris-flow mechanics are complex, the notion of "perfect" debris-flow behavior is not entirely illusory.

Appendix A: Derivation of Equation (3)

[116] To obtain the depth-averaged pore pressure evolution equation (3), we begin with a more conventional, depth-dependent pore pressure evolution equation derived by *Savage and Iverson* [2003]. We assume that the shallow-flow scaling arguments of *Savage and Iverson* [2003] apply, but unlike those authors we assume that the debris is fully saturated with liquid. We also employ total pore pressure p and total normal stress σ as basic variables in place of the excess pore pressure and effective normal stress used by *Savage and Iverson* [2003], and with these substitutions, their equation (18) can be expressed as:

$$\frac{dp}{dt} - D\frac{\partial^2 p}{\partial y^2} = \frac{d\sigma}{dt} + \frac{y}{h}\frac{dh}{dt}\frac{\partial(\sigma - p)}{\partial y} \tag{A1}$$

Here $d/dt = \partial/\partial t + v\partial/\partial x$ is a Lagrangian time derivative in a reference frame moving with the depth-averaged flow velocity v, $\sigma = \rho g(h - y)\cos\theta$ is the y-direction total normal stress due to the weight of the debris, and $\sigma - p$ is the effective stress as defined by *Terzaghi* [1925]. The factor $(y/h)(dh/dt)$ that multiplies $\sigma - p$ is a surrogate for the debris-flow velocity component in the y direction [*Savage and Iverson*, 2003], and as a result, the final term in (A1) represents advective transfer of effective stress in the y direction as the debris-flow thickness changes. Together, the terms on the right-hand side of (A1) represent all forcing effects caused by changes in debris-flow thickness.

[117] The objective of depth integration is to remove the y derivatives from (A1) and thereby reduce the equation to a one-dimensional form in which the dependent variable is the basal pore fluid pressure, $p_{bed}(x, t)$, rather than $p(x, y, t)$. Depth integration of (A1) is accomplished term-by-term using Leibniz' theorem [*Abramowitz and Stegun*, 1964, p. 11] and applying the free-surface boundary condition $p(h) = \sigma(h) = 0$, yielding

$$\frac{d(\overline{p}h)}{dt} - D\left[\left.\frac{\partial p}{\partial y}\right|_{y=h} + \rho_f g\cos\theta\right] = \frac{d(\overline{\sigma}h)}{dt} - (\overline{\sigma} - \overline{p})\frac{dh}{dt} \tag{A2}$$

Here overbars denote depth-averaged values of variables. The term $\rho_f g\cos\theta$ arises from depth-integrating the pore pressure diffusion term in (A1) while applying a zero-flux basal boundary condition that requires the pore pressure gradient at the bed to remain hydrostatic: $[\partial p/\partial y]_{y=0} = -\rho_f g\cos\theta$. The last term in (A2) arises from depth-integrating the last term in (A1) by parts. This term cancels some other terms and thereby reduces (A2) to

$$\frac{d\overline{p}}{dt} - \frac{D}{h}\left[\left.\frac{\partial p}{\partial y}\right|_{y=h} + \rho_f g\cos\theta\right] = \frac{d\overline{\sigma}}{dt} \tag{A3}$$

This equation is exact in a depth-averaged sense, but it retains a y derivative and involves two pore pressure variables, p and $\overline{p}$, rather than the single desired variable, p_{bed}.

[118] To express (A3) in terms of p_{bed}, approximations of $\overline{p}$ and $[\partial p/\partial y]_{y=h}$ are necessary. We use first-order approximations that assume p varies linearly with depth, ranging from $p = p_{bed}$ at $y = 0$ to $p = 0$ at $y = h$, yielding

$$\overline{p} \approx \frac{1}{2} p_{bed} \qquad \left.\frac{\partial p}{\partial y}\right|_{y=h} \approx -\frac{p_{bed}}{h} \tag{A4}$$

Higher order (in y/h) approximations of these quantities allow for nonlinearity of the pore pressure profile, particularly near the bed [*Savage and Iverson*, 2003], but such details complicate the results without revealing effects of fundamental importance here, and we omit them for the sake of brevity. Furthermore, because we treat ρ as a depth-averaged quantity, the depth-averaged normal stress in (A3) can be expressed as:

$$\overline{\sigma} = g\cos\theta \frac{1}{h}\int_0^h \rho(h-y)dy = \frac{1}{2}\rho g h \cos\theta \tag{A5}$$

Substitution of (A4) and (A5) into (A3) yields the final form of the pore pressure evolution equation (3) in the main text.

Appendix B: Normalized Model Equations

[119] Substitution of the scaled variables $x^* = x/L$, $t^* = t/\sqrt{L/g}$, $v^* = v/\sqrt{gL}$, $h^* = h/H$, $\rho^* = \rho/\rho_0$, $p^*_{bed} = p_{bed}/\rho_0 g h \cos\theta$ in equations (1)–(3) yields normalized versions of the equations, which contain only the dimensionless parameters listed in (9):

$$\frac{dh^*}{dt^*} = -h^*\frac{\partial v^*}{\partial x^*} - \frac{h^*}{\rho^*}\frac{d\rho^*}{dt^*} \tag{B1}$$

$$\begin{aligned}\rho^* h^* \frac{dv^*}{dt^*} = {} & \rho^* h^*\left[\sin\theta - \kappa\varepsilon\cos\theta\frac{\partial h^*}{\partial x^*}\right] \\ & - h^*(1-\kappa)\varepsilon\cos\theta\left(\frac{\partial p^*_{bed}}{\partial x^*}\right) \\ & - \left[\frac{\tau_s}{\rho_0 g H} + \frac{\tau_y}{\rho_0 g H} + \frac{1}{\varepsilon}\frac{\mu}{\rho_0 H\sqrt{gL}}\frac{v^*}{h^*}\right]\end{aligned} \tag{B2}$$

$$\frac{dp^*_{bed}}{dt^*} = -2\frac{\sqrt{L/g}}{H^2/D}\left[\frac{p^*_{bed}}{h^{*2}} - \frac{\rho_f}{\rho_0 h^*}\right] + \frac{d(\rho^* h^*)}{dt^*} \tag{B3}$$

Appendix C: Measurement Techniques for Sediment Properties and Water Budgets

[120] Our angle-of repose measurements used the tilt-table apparatus pictured in Figure C1. The table was equipped with a screw drive used to gradually increase the angle of inclination of a rectangular slab of dried sediment until sliding occurred. The sediment rested on either smooth concrete like that of the debris-flow flume bed prior to 2000 or bumpy concrete tiles like those installed on the flume bed in 2000. In tests used to measure internal angles of repose, the bed roughness was supplemented by installing cross-baffles that inhibited basal sliding. Advantages of the tilt-table tests were that they could produce a nearly one-dimensional, statically determinate state of stress in the sediment slabs, and that the gravitationally imposed confining stress was comparable to the typical gravitational stresses in our experimental debris flows (~2 kPa). A disadvantage of the tests was that determination of failure involved some judgment. For our purposes, we deemed that widespread motion of the sediment slab (rather than avalanching of small clusters of grains) constituted failure, and this criterion yielded results that were quite reproducible (Table 2).

[121] Our bulk density measurements of static sediment loaded behind the flume headgate employed an excavation method similar in principle to standard sand-cone or rubber-bladder methods [e.g., *Blake*, 1965], but distinguished by the fact that we backfilled our excavations with spherical ~2 mm steel shot and then extracted the shot using a magnet. Sample volumes determined by weighing the shot (which had a very consistent weight per unit volume) were generally about 1000 cm^3. Results of subsequent oven-drying and weighing of the sampled sediment yielded the dry bulk densities listed in Table 3.

[122] Our measurements of hydraulic permeability employed sediment specimens of about 3500 cm^3 volume placed in a standard compaction permeameter, compressed to varying degrees by applying static loads, saturated with water, and then subjected to diverse upward head gradients until a steady water discharge occurred. These tests revealed almost perfectly Darcian behavior in which the discharge was proportional to the imposed hydraulic head gradient. For both the SG and SGM mixtures, Darcian permeabilities (k) inferred from these tests increased approximately exponentially as a function of porosity, such that $k = k_0 \exp(an)$, where k_0 is a reference permeability and a is a parameter varying from about 10 to 30 [*Iverson*, 1997; *Major et al.*, 1997]. For the most relevant range of porosities, k values for the SG were about ten times larger than for the SGM (Table 3).

[123] Hydraulic diffusivity, D (also called the consolidation coefficient) was a more difficult parameter to measure. *Major* [1996], *Major et al.* [1997], *Major and Iverson* [1999], and *Major* [2000] discuss the details of our various approaches, which entailed both computation of D using the measured values of k and the secant Young's modulus E determined from triaxial strain tests, and also direct inference of D by fitting theoretical consolidation curves to measurements of pore pressure evolution in slurries in test cells and in experimental debris-flow deposits. In all cases, the D values for SGM were smaller than those for SG, and the measured D values for slurries were at least 100 times smaller than D values calculated from the k and E values of the source sediment [*Major et al.*, 1997] (Table 3).

[124] The water content of our sediment mixtures depended on two components: the native water in the sediment when it was loaded behind the headgate, and water we subsequently added by metered sprinkling and subsurface feeding. We determined the weight percent water content of sediment in its native state by sampling and weighing, as described above, and we converted this weight percent to volumetric water content by using standard formulas in conjunction with the sediment porosities computed from dry bulk densities (Table 2). The net water we added to the sediment included both pore water and the water in the small pond upslope of the sediment prism, but excluded water that

Figure C1. Photograph of tilt-table apparatus configured for measuring static internal friction of dry sediment. Sediment slab is 61 cm long, 37 cm wide, and 6 cm thick.

leaked through or over the headgate and was captured and measured using a system installed for that purpose.

[125] Although we know that about 3.3 m^3 of water was typically contained in our 9.7 m^3 sediment masses (Table 3), and that the initial sediment porosity was typically 0.36–0.39 (Table 2), our inferences about the degree of sediment saturation are complicated by sediment compaction that occurred during water application. Such compaction occurs almost universally when relatively dry, loosely packed sediment is wetted, but the compaction we observed was difficult to measure accurately because the initially planar sediment surface became irregular during wetting and settlement, and the only readily accessible points for measuring settlement were along the flume sidewalls. There, measurements indicated that volumetric compaction averaged about 2 percent.

[126] To account for compaction during wetting, we reduced the sediment volume by 2 percent before calculating the volumetric saturation and sediment wet bulk density. This reduction yielded mean saturation estimates of 93 percent for the SGM experiments and 96 to 97 percent for the SG experiments (Table 2), values consistent with the fact that some entrapped air bubbles were nearly impossible to dislodge from the water-laden sediment. The same 2 percent volume reduction was used to obtain our estimates of the mean wet bulk density of the sediment loaded behind the headgate (Table 2).

[127] We measured the wet bulk density of slurry-like sediment deposited in the runout area at the conclusion of experiments by carefully inserting a thin-walled steel cylinder 15 cm in diameter through the deposit until it contacted the underlying concrete bed, then measuring the local deposit thickness and excavating and weighing all the enclosed debris. Grain-size segregation resulted in concentrations of unsaturated, gravel-rich debris at deposit margins, and we measured the dry bulk density of this debris by using the same excavation method we used to measure sediment loaded behind the headgate.

[128] **Acknowledgments.** We are indebted to many colleagues who assisted with parts of the experimental program at the USGS debris-flow flume from 1994 to 2004. Sustained contributions were made by Tony Bequette, Roger Denlinger, Julia Griswold, Kevin Hadley, Jon Major, Mark Reid, Kelly Swinford, and Jim Vallance. We are also indebted to those who facilitated design, construction, and continuing experimentation at the flume, particularly John Costa, Franz Rad, Fred Swanson, Art McKee, John Cissell, Lisa Anheluk, Jerry Stevenson, and Lynn Burditt. Staff at the H.J. Andrews Experimental Forest cordially hosted us during our flume work and helped us meet countless small exigencies. Mark Reid, Jonathan Godt, Christophe Ancey, and two anonymous referees provided helpful reviews of our manuscript.

References

Abramowitz, M., and I. A. Stegun (Eds.) (1964), *Handbook of Mathematical Functions with Formulas, Graphs, and Mathematical Tables*, U.S. Dep. of Comm. Natl. Bur. of Stand., Washington, D. C.

Allen, P. A. (1997), *Earth Surface Processes*, 416 p., Blackwell Sci., Malden, Mass.

Alshibli, K. A., S. Sture, N. C. Costes, M. L. Frank, M. R. Lankton, S. N. Batiste, and R. A. Swanson (2000), Assessment of localized deformations in sand using X-ray computed tomography, *Geotech. Test. J.*, *23*, 274–299.

Ancey, C. (2001), Role of lubricated contacts in concentrated polydisperse suspensions, *J. Rheol.*, *45*, 1421–1439, doi:10.1122/1.1413504.

Ancey, C., and P. Evesque (2000), Frictional-collisional regime for granular suspension flows down an inclined channel, *Phys. Rev. E*, *62*, 8349–8360, doi:10.1103/PhysRevE.62.8349.

Ancey, C., R. M. Iverson, M. Rentschler, and R. P. Denlinger (2008), An exact solution for ideal dam-break floods on steep slopes, *Water Resour. Res.*, *44*, W01430, doi:10.1029/2007WR006353.

Bagnold, R. A. (1954), Experiments on a gravity-free dispersion of large solid spheres in a Newtonian fluid under shear, *Proc. R. Soc. London, Ser. A*, *225*, 49–63, doi:10.1098/rspa.1954.0186.

Bendat, J. S., and A. G. Piersol (1986), *Random Data, Analysis and Measurement Procedures*, 2nd ed., Wiley, New York.

Berzi, D., and J. T. Jenkins (2008), A theoretical analysis of free-surface flows of saturated granular-liquid mixtures, *J. Fluid Mech.*, *608*, 393–410, doi:10.1017/S0022112008002401.

Bingham, E. C., and H. Green (1919), Paint, a plastic material and not a viscous liquid, the measurement of its mobility and yield value, *Proc. Am. Soc. Test. Mater.*, *19*, 640–664.

Blake, G. R. (1965), Bulk density, in *Methods of Soil Analysis, Part 1*, edited by C. A. Black et al., pp. 374–390, Am. Soc. of Agron., Madison, Wis.

Burroughs, S. M., and S. F. Tebbens (2001), Upper-truncated power laws in natural systems, *Pure Appl. Geophys.*, *158*, 741–757, doi:10.1007/PL00001202.

Coulomb, C. A. (1773), Sur une application des règles de maximix & minimis à quelques problèms de stique, relatifs à l' architecture, *Mém. Math. Phys. Acad. R. Sci.*, *7*, 343–382.

Coussot, P., and S. Proust (1996), Slow, unconfined spreading of a mudflow, *J. Geophys. Res.*, *101*, 25,217–25,229, doi:10.1029/96JB02486.

DeNatale, J. S., R. M. Iverson, J. J. Major, R. G. LaHusen, G. L. Fiegel, and J. D. Duffy (1999), Experimental testing of flexible barriers for containment of debris flows, *U.S. Geol. Surv. Open File Rep., 99–205*, 38 p.

Denlinger, R. P., and R. M. Iverson (2001), Flow of variably fluidized granular masses across three-dimensional terrain: 2. Numerical predictions and experimental tests, *J. Geophys. Res.*, *106*, 553–566, doi:10.1029/2000JB900330.

Denlinger, R. P., and R. M. Iverson (2004), Granular avalanches across irregular three-dimensional terrain: 1. Theory and Computation, *J. Geophys. Res.*, *109*, F01014, doi:10.1029/2003JF000085.

Fannin, R. J., A. Eliadoran, and J. M. T. Wilkinson (2005), Shear strength of cohesionless soils at low stress, *Geotechnique*, *55*, 467–478, doi:10.1680/geot.2005.55.6.467.

Forterre, Y., and O. Pouliquen (2008), Flows of dense granular media, *Annu. Rev. Fluid Mech.*, *40*, 1–24, doi:10.1146/annurev.fluid.40.111406.102142.

GDR MiDi group (2004), On dense granular flows, *Eur. Phys. J. E*, *14*, 127–135.

Goldhirsch, I. (2003), Rapid Granular Flows, *Annu. Rev. Fluid Mech.*, *35*, 267–293, doi:10.1146/annurev.fluid.35.101101.161114.

Gray, J. M. N. T., and C. Ancey (2009), Segregation, recirculation and deposition of coarse particles near two-dimensional avalanche fronts, *J. Fluid Mech.*, *629*, 387–423, doi:10.1017/S0022112009006466.

Hunt, M. L., R. Zenit, C. S. Campbell, and C. E. Brennen (2002), Revisiting the 1954 suspension experiments of R.A. Bagnold, *J. Fluid Mech.*, *452*, 1–24, doi:10.1017/S0022112001006577.

Iverson, R. M. (1997), The physics of debris flows, *Rev. Geophys.*, *35*, 245–296, doi:10.1029/97RG00426.
Iverson, R. M. (2003), The debris-flow rheology myth, in *Debris-flow Hazards Mitigation: Mechanics, Prediction, and Assessment*, vol. 1, edited by D. Rickenmann and C. L. Chen, pp. 303–314, Millpress, Rotterdam, Netherlands.
Iverson, R. M. (2009), Elements of an improved model of debris-flow motion, in *Powders and Grains 2009*, edited by M. Nakagawa and S. Luding, pp. 9–16, Am. Inst. of Phys., Melville, New York.
Iverson, R. M., and R. P. Denlinger (2001), Flow of variably fluidized granular masses across three-dimensional terrain: 1. Coulomb mixture theory, *J. Geophys. Res.*, *106*, 537–552, doi:10.1029/2000JB900329.
Iverson, R. M., and R. G. LaHusen (1989), Dynamic pore-pressure fluctuations in rapidly shearing granular materials, *Science*, *246*, 796–799, doi:10.1126/science.246.4931.796.
Iverson, R. M., and J. W. Vallance (2001), New views of granular mass flows, *Geology*, *29*, 115–118, doi:10.1130/0091-7613(2001)029<0115:NVOGMF>2.0.CO;2.
Iverson, R. M., M. E. Reid, and R. G. LaHusen (1997), Debris-flow mobilization from landslides, *Annu. Rev. Earth Planet. Sci.*, *25*, 85–138, doi:10.1146/annurev.earth.25.1.85.
Iverson, R. M., M. E. Reid, N. R. Iverson, R. G. LaHusen, M. Logan, J. E. Mann, and D. L. Brien (2000), Acute sensitivity of landslide rates to initial soil porosity, *Science*, *290*, 513–516, doi:10.1126/science.290.5491.513.
Iverson, R. M., M. Logan, and R. P. Denlinger (2004), Granular avalanches across irregular three-dimensional terrain: 2. Experimental tests, *J. Geophys. Res.*, *109*, F01015, doi:10.1029/2003JF000084.
Johnson, A. M. (1970), *Physical Processes in Geology*, Freeman Cooper, San Francisco, Calif.
Kowalski, J. (2008), Two-phase modeling of debris flow, D.Sc. dissertation, ETH Zurich, Zurich, Switzerland.
Lambe, T. W., and R. V. Whitman (1979), *Soil Mechanics, SI Version*, Wiley, New York.
Logan, M., and R. M. Iverson (2007), Video documentation of experiments at the USGS debris-flow flume, 1992–2006, *U.S. Geol. Surv. Open File Rep., 2007-1315*. (Available at http://pubs.usgs.gov/of/2007/1315/).
Major, J. J. (1996), Experimental studies of deposition by debris flows: Process, characteristics of deposits, and effects of pore-fluid pressure, Ph.D. dissertation, Univ. of Washington, Seattle, Wash.
Major, J. J. (1997), Depositional processes in large-scale debris-flow experiments, *J. Geol.*, *105*, 345–366, doi:10.1086/515930.
Major, J. J. (1998), Pebble orientation on large, experimental debris-flow deposits, *Sediment. Geol.*, *117*, 151–164, doi:10.1016/S0037-0738(98)00014-1.
Major, J. J. (2000), Gravity-driven consolidation of granular slurries: Implications for debris-flow deposition and deposit characteristics, *J. Sediment. Res.*, *70*, 64–83, doi:10.1306/2DC408FF-0E47-11D7-8643000102C1865D.
Major, J. J., and R. M. Iverson (1999), Debris-flow deposition-effects of pore-fluid pressure and friction concentrated at flow margins, *Geol. Soc. Am. Bull.*, *111*, 1424–1434, doi:10.1130/0016-7606(1999)111<1424:DFDEOP>2.3.CO;2.
Major, J. J., and T. C. Pierson (1992), Debris flow rheology: Experimental analysis of fine-grained slurries, *Water Resour. Res.*, *28*, 841–857, doi:10.1029/91WR02834.
Major, J. J., R. M. Iverson, D. F. McTigue, S. Macias, and B. K. Fiedorowicz (1997), Geotechnical properties of debris-flow sediments and slurries, in *Debris-flow Hazards Mitigation: Mechanics, Prediction, and Assessment*, edited by C. L. Chen, pp. 249–259, Am. Soc. of Civ. Eng., New York.
McArdell, B. W., P. Bartelt, and J. Kowalski (2007), Field observations of basal forces and fluid pore pressures in a debris flow, *Geophys. Res. Lett.*, *34*, L07406, doi:10.1029/2006GL029183.
O'Brien, J. S., and P. Y. Julien (1988), Laboratory analysis of mudflow properties, *J. Hydraul. Eng.*, *114*, 877–887, doi:10.1061/(ASCE)0733-9429(1988)114:8(877).
Pailha, M., and O. Pouliquen (2009), A two-phase flow description of the initiation of underwater granular avalanches, *J. Fluid Mech.*, *633*, doi:10.1017/S0022112009007460.
Parsons, J. D., K. X. Whipple, and A. Simioni (2001), Experimental study of the grain-flow, fluid-mud transition in debris flows, *J. Geol.*, *109*, 427–447, doi:10.1086/320798.
Pierson, T. C. (1986), Flow behavior of channelized debris flows, Mount St. Helens, Washington, in *Hillslope Processes*, edited by A. D. Abrahams, pp. 269–296, Allen and Unwin, Boston, Mass.
Press, W. H., B. P. Flannery, S. A. Teukolsky, and W. T. Vettering (1986), *Numerical Recipes*, Cambridge Univ. Press, Cambridge, U. K.
Rankine, W. J. M. (1857), On the stability of loose earth, *Philos. Trans. R. Soc. London*, *147*, 9–27.
Reid, M. E., R. G. LaHusen, and R. M. Iverson (1997), Debris-flow initiation experiments using diverse hydrologic triggers, in *Debris-flow Hazards Mitigation: Mechanics, Prediction, and Assessment*, edited by C.-L. Chen, pp. 1–11, Am. Soc. Civ. Eng., New York.
Ritter, D. F., R. C. Kochle, and J. R. Miller (2002), *Process Geomorphology*, 4th ed., Waveland Press, Long Grove, Ill.
Savage, S. B., and K. Hutter (1989), The motion of a finite mass of granular material down a rough incline, *J. Fluid Mech.*, *199*, 177–215, doi:10.1017/S0022112089000340.
Savage, S. B., and R. M. Iverson (2003), Surge dynamics coupled to pore-pressure evolution in debris flows, in *Debris-flow Hazards Mitigation: Mechanics, Prediction, and Assessment*, vol. 1, edited by D. Rickenmann and C.-L. Chen, pp. 503–514, Millpress, Rotterdam, Netherlands.
Schonfeld, B. (1996), Roll waves in granular flows and debris flows, M.S. thesis, Dep. of Civ. Eng. and Appl. Mech., McGill Univ., Montreal, Canada.
Sharp, R. P., and L. H. Nobles (1953), Mudflow of 1941 at Wrightwood, southern California, *Geol. Soc. Am. Bull.*, *64*, 547–560, doi:10.1130/0016-7606(1953)64[547:MOAWSC]2.0.CO;2.
Stiny, J. (1910), *Debris Flows*, translated by M. Jakob and N. Skermer, Innsbruck, Austria.
Takahashi, T. (1981), Debris flow, *Ann. Rev. Fluid Mech.*, *13*, 57–77.
Takahashi, T. (1991), *Debris Flow*, Balkema, Rotterdam, Netherlands.
Terzaghi, K. (1925), *Erdbaumechanik*, Franz Deuticke, Vienna.
Thornton, A. R., and J. M. N. T. Gray (2008), Breaking size-segregation waves and particle recirculation in granular avalanches, *J. Fluid Mech.*, *596*, 261–284, doi:10.1017/S0022112007009445.
Turcotte, D. L. (1992), *Fractals and Chaos in Geology and Geophysics*, Cambridge Univ. Press, Cambridge, U. K.
Zanuttigh, B., and A. Lamberti (2007), Instability and surge development in debris flows, *Rev. Geophys.*, *45*, RG3006, doi:10.1029/2005RG000175.

M. Berti, Dipartimento di Scienze della Terra e Geologico-Ambientali, Università di Bologna, Via Zamboni 67, I- 40126 Bologna, Italy.
R. M. Iverson, R. G. LaHusen, and M. Logan, U.S. Geological Survey, Cascade Volcano Observatory, 1300 SE Cardinal Court, #100, Vancouver, WA 98683, USA. (riverson@usgs.gov)